Pediatric Neurology 96 (2019) 7–23

Contents lists available at ScienceDirect

Pediatric Neurology

journal homepage: www.elsevier.com/locate/pnu

Topical Review

Recent Advances in Pediatric Brain, Spine, and Neuromuscular Magnetic Resonance Imaging Techniques

Ramkumar Krishnamurthy, PhD [a], Danny J.J. Wang, PhD [b], Barbara Cervantes, PhD [c], Aaron McAllister, MD [a], Eric Nelson, PhD [d], Dimitrios C. Karampinos, PhD [c], Houchun Harry Hu, PhD [a, *]

[a] *Radiology, Nationwide Children's Hospital, Columbus, Ohio*
[b] *Keck School of Medicine, University of Southern California, Los Angeles, California*
[c] *Department of Diagnostic and Interventional Radiology, Technische Universität München, Munich, Germany*
[d] *Center for Biobehavioral Health, Nationwide Children's Hospital, Columbus, Ohio*

ARTICLE INFO

Article history:
Received 1 July 2018
Accepted 3 March 2019
Available online 12 March 2019

Keywords:
Neurography
Arterial spin labeling
Amide proton transfer
Neuromuscular imaging
Compressed sensing
Simultaneous multislice
Synthetic MRI
MR fingerprinting

ABSTRACT

Magnetic resonance imaging (MRI) is a powerful radiologic tool with the ability to generate a variety of proton-based signal contrast from tissues. Owing to this immense flexibility in signal generation, new MRI techniques are constantly being developed, tested, and optimized for clinical utility. In addition, the safe and nonionizing nature of MRI makes it a suitable modality for imaging in children. In this review article, we summarize a few of the most popular advances in MRI techniques in recent years. In particular, we highlight how these new developments have affected brain, spine, and neuromuscular imaging and focus on their applications in pediatric patients. In the first part of the review, we discuss new approaches such as multiphase and multidelay arterial spin labeling for quantitative perfusion and angiography of the brain, amide proton transfer MRI of the brain, MRI of brachial plexus and lumbar plexus nerves (i.e., neurography), and T2 mapping and fat characterization in neuromuscular diseases. In the second part of the review, we focus on describing new data acquisition strategies in accelerated MRI aimed collectively at reducing the scan time, including simultaneous multislice imaging, compressed sensing, synthetic MRI, and magnetic resonance fingerprinting. In discussing the aforementioned, the review also summarizes the advantages and disadvantages of each method and their current state of commercial availability from MRI vendors.

Introduction

Magnetic resonance imaging's (MRI) ability to generate flexible soft tissue contrast that is superior to any other existing imaging tool has made it a widely used modality for evaluating brain, spine, and neuromuscular pathology. In particular, MRI is attractive in pediatric imaging because of its lack of ionizing radiation, which makes it a suitable modality for multiple scans and repeat examination in longitudinal follow-up studies. For clinicians, appropriately performed MRI examinations provide a breadth and depth of useful clinical information and add diagnostic confidence.[1] Driven by advances in hardware and software, the field of MRI is constantly evolving, with new signal contrast mechanisms and data acquisition strategies continuously being rapidly developed and introduced into clinical practice.[2,3] The purpose of this article is to summarize for the pediatric neurologist some of the most recent MRI applications and techniques in neuroimaging over the past five years.

In the first part of the review, several new applications that manipulate the proton (water) signal of tissues and blood to generate new signal contrast are discussed, including multiphase or multidelay arterial spin labeling (ASL), amide proton transfer (APT) MRI of the brain, MRI of brachial plexus and lumbar plexus nerves (i.e., neurography), and T2 mapping and fat characterization in neuromuscular diseases. Clinical examples in pediatric and

---

Conflicts of interest: NCH receives research support from GE Healthcare and Siemens Healthcare in the form of works-in-progress MRI software. Danny JJ Wang is a shareholder of Translational MRI LLC which provided the software for post-processing of multi-delay pCASL data.

* Communications should be addressed to: Hu; Department of Radiology; Nationwide Children's Hospital; 700 Children's Drive; Columbus, OH, 43205.
E-mail address: Houchun.hu@nationwidechildrens.org (H.H. Hu).

https://doi.org/10.1016/j.pediatrneurol.2019.03.001
0887-8994/

adolescent patients with pathology are shown for each method. In the second part of the review, the content shifts to a description of new data acquisition strategies in MRI that are aimed to accelerate speed and reduce scan time. In pediatric applications, accelerated imaging is particularly attractive as it can reduce both the presence of motion-related image artifacts and the need for sedation.[4-6] These acceleration methods include simultaneous multislice imaging, compressed sensing, synthetic MRI, and magnetic resonance (MR) fingerprinting. In both sections, the review also provides a summary of the advantages and disadvantages to complement each technique along with their commercial availability and most commonly used applications. For each technique, appropriate references are given for the interested reader. Last, the article concludes with some directions of future research. Tables 1 and 2 list the current availability, primary usage, information on scan duration and image resolution, and some advantages and limitations of each described technique.

Our intent is to provide a straightforward overview of some of the most popular advanced MRI techniques. We hope that the content stimulates the reader's interest with a greater understanding and appreciation of MRI's flexibility and provides them with useful knowledge to facilitate consultations with radiologists and medical physicists in determining the most appropriate clinical care for their patients. This review is not intended to be comprehensive, and the interested reader is referred to additional references in the literature.

Brain and spine techniques and applications

Single-phase and multiphase arterial spin labeling

Single-phase or single-delay ASL MRI refers to the use of a single pulse labeling delay (PLD) time settings during an examination. The PLD signifies the time between the labeling of blood signal, typically at the level of the carotid arteries below the bifurcation, and the time when data acquisition starts at the imaging volume upstream, typically 75 to 90 mm away in distance. In conventional single-delay ASL experiments wherein one PLD is used, the technique provides clinicians an approach to noninvasively quantify cerebral blood flow (CBF) in units of mL/100 g/min. Fundamentally, ASL utilizes magnetically labeled arterial blood water as an endogenous tracer.[7] One key advantage of ASL is that it involves no intravenous injection of contrast solution like gadolinium-based agents.[7] Therefore an ASL scan can easily be repeated, if necessary.

ASL is particularly suitable for measuring CBF in pediatric populations, for example, in patients with moyamoya disease[8] or sickle cell disease.[9] In addition, ASL has also been used to establish normative values during growth and development.[10,11] As CBF is normally coupled to glucose metabolism and neuronal activity,[12,13] it is a viable surrogate marker of brain function. ASL-derived CBF measurements have been validated using ^{15}O-water positron emission tomography[14-17] and have been shown to provide complementary information to ^{18}F-glucose measurements of cerebral glucose metabolism.[18-20] CBF is also a promising imaging biomarker for assessing functional brain development in both healthy populations and those with developmental disorders. Studies in children have demonstrated an age-related increase in CBF from neonates to toddlers, followed by a tapering of CBF from childhood to adulthood.[21-24] This developmental trajectory of CBF is consistent with findings from nuclear medicine approaches.[25,26] Recent studies assessing regional CBF with adjustment of variations in gray matter density showed that the relationship between gray-matter-density-adjusted CBF and age can be characterized by an inverted U-shape followed by a U-shaped trajectory in most brain regions throughout childhood and adolescence.[27,28] A prominent gender difference in the developmental trajectories of CBF has also been reported in a large cohort of 922 individuals aged between eight and 22 years.[29]

TABLE 1.
Summary of Neuro and Neuromuscular MRI Techniques Discussed in This Review

Technique	Commercial Availability	Primary Usage	Typical Scan Time/Spatial Resolution	Advantages Over Existing Practices	Limitations
Arterial spin labeling (multidelay/ multiphase)	Not available as commercial product, but feasibility has been demonstrated on Siemens, Philips, and General Electric MRI platforms	Brain perfusion: cerebral blood flow, arterial transit time, cerebral blood volume, especially in patients with suspected circulation asymmetry	3D scan, 4-6 minutes for whole-brain coverage/2-4 mm in-plane 3- to 5-mm slices	No gadolinium contrast agents, noninvasive, repeatable	Moderate postprocessing required Limited signal-to-noise ratio, long scan times due to multiple averages, sensitive to labeling and delay timing parameters and patient motion
Amide proton transfer	Available from major vendors on newest MRI systems as work-in-progress packages	Magnetization transfer-based assessment of tumor protein content	2D or 3D scan, dependent on interrogating region, but typically 5-7 minutes/ 2-4 mm in-plane, >5-mm slices	Unique signal contrast mechanism No gadolinium contrast agents, noninvasive, repeatable	Sensitive to magnetic field inhomogeneity and patient motion, long scan times sensitive to motion Moderate postprocessing required
Neurography	Available from major vendors on newest MRI systems as product or work-in-progress packages	Delineation of nerve roots, trunks, divisions, and cords	3D scan 4-5 minutes for brachial plexus, 5-7 minutes for lumbar plexus/0.7-1.5 mm in-plane, 1 to 1.5-mm slices	New methods provide high nerve-to-tissue contrast with uniform fat and fluid suppression, isotropic voxels allow arbitrary reformats	3D fast/turbo spin echo sequences can lead to high specific absorption ratios for long scans, long scan times Sensitive to motion
Proton density fat fraction mapping and T2 mapping	Available from major vendors	Organ steatosis, tissue percent fat quantification, edema, fibrosis	2D or 3D scan, 3-5 minutes per upper limb or lower extremity coverage/1-2 mm in-plane 2- to 5-mm slices	Provides reproducible and repeatable quantitative measurements over qualitative T1- and T2-weighted scans	Fat fraction mapping sensitive to magnetic field inhomogeneity, T2 mapping sensitive to motion, light postprocessing required

Abbreviations:
2D = Two dimensional
3D = Three-dimensional
MRI = Magnetic resonance imaging

TABLE 2.
Summary of Accelerated Data Acquisition MRI Techniques Discussed in This Review

Technique	Commercial Availability	Primary Usage	Comments
Simultaneous multislice	Available from major vendors on newest MRI systems as product or work-in-progress packages	Widely used in acceleration of data acquisition speed in functional MRI and diffusion tractography brain imaging	No signal-to-ratio loss when compared with conventional methods, sensitive to magnetic field inhomogeneity, two- to fourfold acceleration
Compressed sensing	Available from major vendors on newest MRI systems as product or work-in-progress packages	Widely used in acceleration of data acquisition speed in all anatomies, most notably in spectroscopy, angiography, flow, and dynamic cardiovascular applications	High-powered postprocessing computers needed, reconstruction parameters tend to be application specific, atypical artifacts and signal-to-noise ratio may manifest due to inappropriate parameters
Synthetic MRI and MR fingerprinting	Synthetic MRI available from major vendors on newest MRI systems as product or work-in-progress packages MR fingerprinting currently not available	Initial demonstration and utility in brain imaging, research in cardiac, body, and musculoskeletal applications being pursued	Synthetic MRI feasibility has been established, limited literature reports on clinical utility and added-value, additional large-cohort evaluation needed. MR fingerprinting is currently used in research setings.

Abbreviations:
MR = Magnetic resonance
MRI = Magnetic resonance imaging

A pediatric template of brain perfusion has also been established from data in 120 children aged seven to 18 years.[30] The test-retest repeatability of ASL-derived CBF measurements in children has also been established in 22 healthy children aged seven to 17 years using repeated scans two to four weeks apart.[31] In addition, ASL has been used to characterize neural and biological changes in children with genetic or developmental disorders such as congenital heart diseases,[32] pediatric stroke,[33] autism spectrum disorders,[34] adolescent depression,[35] attention-deficit/hyperactivity disorder,[36] and substance use.[37] Two physiologic properties of the pediatric brain also make ASL an attractive tool for perfusion imaging in young populations.[38] Blood flow rates are generally higher in children than in adults (except neonates). Consequently, in children, there is increased perfusion signal contrast. Second, brain water content is higher in children than in adults, which leads to a longer T1 relaxation time of blood water. Consequently, an increase in signal-to-noise ratio (SNR) of ASL images has been reported in children compared with adults.[21]

One limitation of ASL is the relatively low SNR of the magnetically labeled blood water measurements. To address this issue, a recent consensus article by Alsop et al. established a set of standardized ASL image acquisition settings for clinical use.[39] The recommendations were endorsed by the International Society for Magnetic Resonance Medicine Perfusion Study Group and the European ASL in Dementia consortium. The joint panel recommended 3-T MRI, with a pseudocontinuous labeling scheme for generating ASL signal (i.e., pCASL) and a three-dimensional data acquisition with segmented readout, as the optimal strategy. The two most common three-dimensional pulse sequences offered by commercial vendors for pCASL are the hybrid gradient and spin echo approach[40] and the stack-of-spirals approach.[41] The consensus article also recommended pCASL PLDs of 2000 ms for neonates, 1500 ms for children, and 1800 ms for adults.

Another limitation of single-phase ASL is arterial-transit-time (ATT)-related effects. These effects manifest when the selected PLD of the acquisition is significantly mismatched to the underlying physiology. ATT is well defined in people with healthy vasculature. However, even in healthy subjects, distal arteries are affected due to a varied ATT. In cereberovascular disease conditions, ATT is significantly different, leading to an inaccurate PLD.[42,43] Thus the PLD is set incorrectly (usually too short) and is insufficient for allowing enough labeled blood to adequately reach the brain tissue of interest.[44] In such cases, CBF measurements will be inaccurate, as a bulk of the labeled signal will have remained in the feeding arteries. Age-related variations with ATT and asymmetric labeling of blood from imperfect patient positioning and vessel tortuosity further adds to the complexity of ATT effects.[31]

To overcome this limitation from ATT effects, multiphase or multidelay ASL methods have been introduced and are becoming increasingly used in clinical settings.[44-47] With data from multiple PLDs, the technique can provide simultaneously an ATT-corrected CBF map and a quantitative map of the ATT parameter itself.[48] Multidelay ASL has been successfully demonstrated in moyamoya disease,[49] in acute ischemic stroke,[50-52] and in patients with idiopathic generalized epilepsy.[53] Two patient examples of multidelay ASL from the first author's institution are shown in Figs 1 and 2.[54] For whole-brain coverage with approximately 30 to 40 contiguous 4-mm slices, a typical five-phase ASL scan takes four to six minutes to complete, and the scan can be performed independent of sedation and general anesthesia. In infants and small children, the field of view slice number, and labeling offset can be reduced to match the small head size. However, because CBF is low in neonates (~10 mL/100 g/min), more averages are required to improve the SNR of multidelay ASL in this population.

In addition to perfusion quantification, multidelay ASL techniques have also been applied to intracranial angiography. With growing concerns over residual intracranial gadolinium deposition and accumulation in patients who undergo multiple contrast-enhanced MRI examiations[55,56] and the general aversion to intravenous needle placement, nongadolinium MR angiography techniques have gained in popularity,[57,58] especially in pediatric applications.[59] Several exemplary data sets are shown in Fig 3, each requiring approximately five minutes for acquiring the circle of Willis and its perfusion territories. These data support the utility of the technique in patients with vascular pathologies and abnormal flow patterns. As with traditional vessel-selective ASL methods, these dynamic approaches can also selectively target specific principal blood vessels (i.e., carotid arteries) and downstream vascular territories.[60] A recent study by Togao et al. has also compared ASL-based angiography to conventional contrast-enhanced MR angiography.[61]

Some drawbacks of multidelay or multiphase ASL in children include the limited spatial resolution (i.e., large voxel size) and their current availability only as work-in-progress sequences from major MRI vendors. One reason for the limited spatial resolution (see Table 1) is the inherent poorer signal source of ASL. In small children, multidelay ASL provides a useful tissue-level look at regional brain perfusion with typical voxel sizes of 2 × 2 × 4 mm^3. At our institution, we have implemented work-in-progress multidelay ASL sequences on multiple 3-T platforms under research mode.

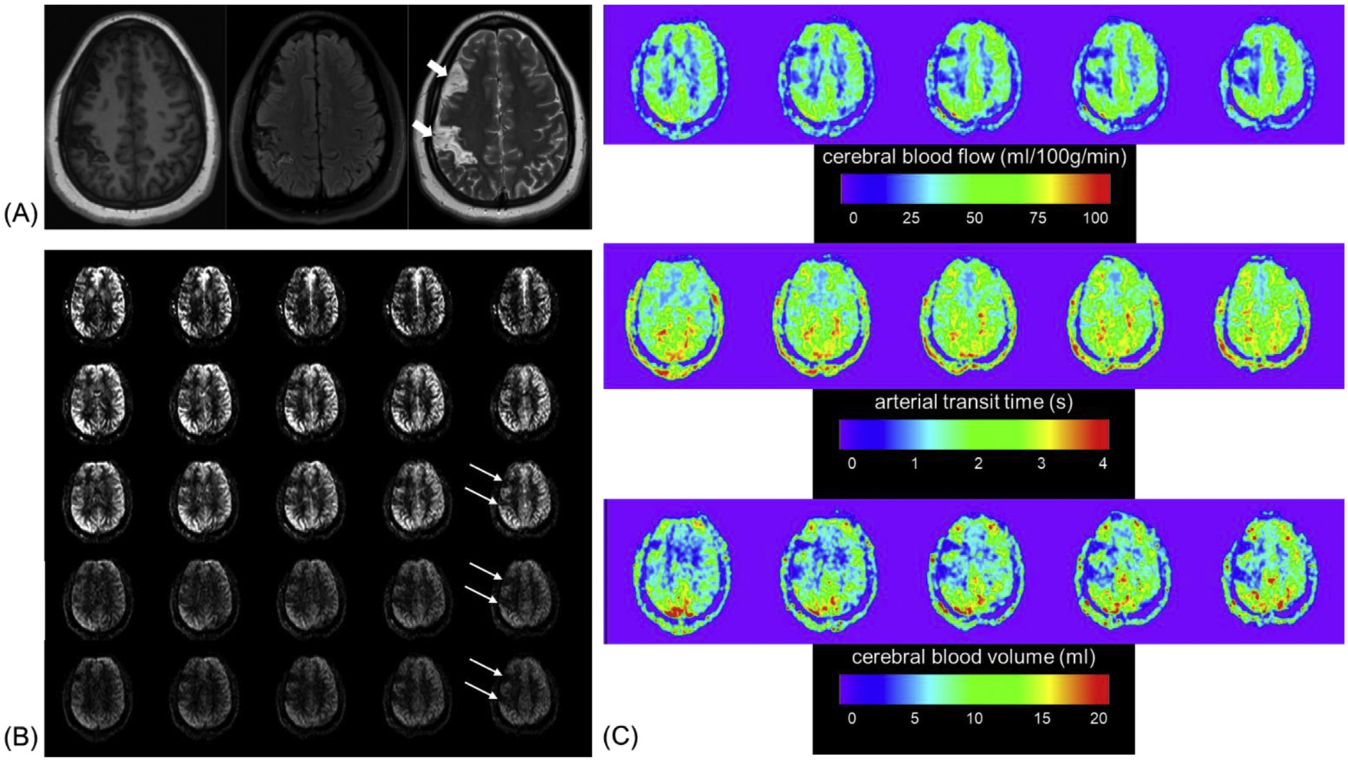

FIGURE 1. Images from a 17-year-old girl with a history of stroke. (A) On T1-weighted (left), fluid-attenuated T2-weighted (middle), and conventional T2-weighted (right) images, there is an area of cystic encephalomalacia (thick arrows). (B) Multiphase arterial spin labeling images with pulse labeling delay (PLD) times of 500 ms (top), 1000 ms, 1500 ms, 2000 ms, and 2500 ms (bottom). (C) Color maps of cerebral blood flow (CBF), arterial transit time, and cerebral blood volume (CBV) derived from the multi-PLD data. The perfusion deficits in the right anterior lateral front lobe can be clearly observed on the longer PLD data (thin arrows) and CBF and CBV maps. The color version of this figure is available in the online edition.

MR neurography

MRI of the peripheral nervous system, including the proximal and distal nerves, is referred to as *magnetic resonance neurography*. MR neurography is emerging as a useful diagnostic tool and noninvasive alternative to nerve conduction evaluation in the assessment of nerve pathologies in both children and adults.[62-66] MR neurography has been used in the diagnosis and treatment of peripheral neuropathy by detecting and characterizing nerve lesions, muscle denervation, neurofibromatosis, and nerve entrapment as well as in providing guidance for perineural injections.[67-72] In recent years, MR neurography has been shown to have a significant impact on the clinical diagnosis and therapeutic procedures of patients with different causes of neuropathy,[64,73,74] and is establishing itself as a promising technique for reducing the number of unnecessary surgeries.[64]

In its current implemented form, MR neurography pulse sequences are a collection of two-and three-dimensional fast or turbo

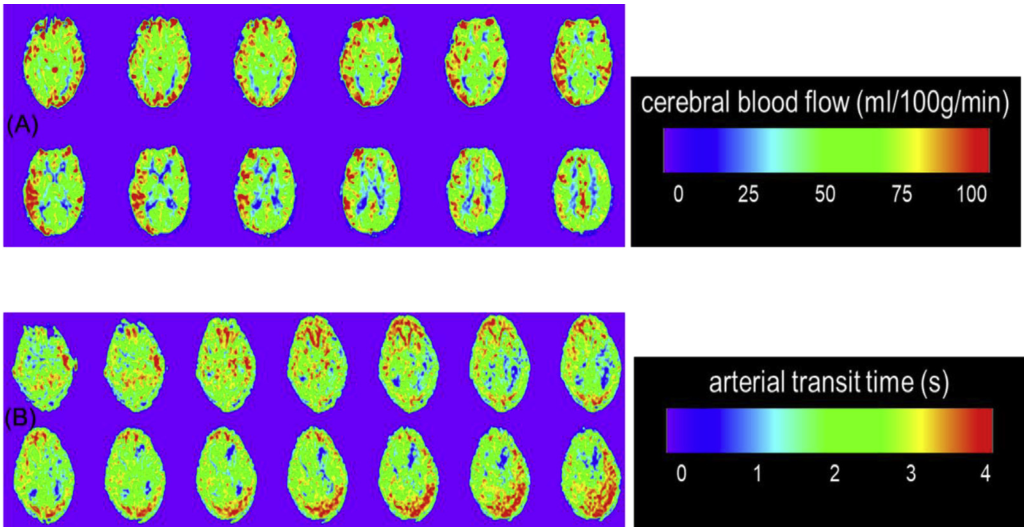

FIGURE 2. (A) Multiphase arterial spin labeling (ASL) cereberal blood flow (CBF) images from a 10-year-old female with a history of rhabdomyosarcoma are shown. Asymmetry in CBF between left and right sides is clearly observed. (B) Multiphase ASL arterial transit time (ATT) images from a seven-year-old girl with a right thalamus mass. Again, asymmetry and delayed ATT are clearly observed. The color version of this figure is available in the online edition.

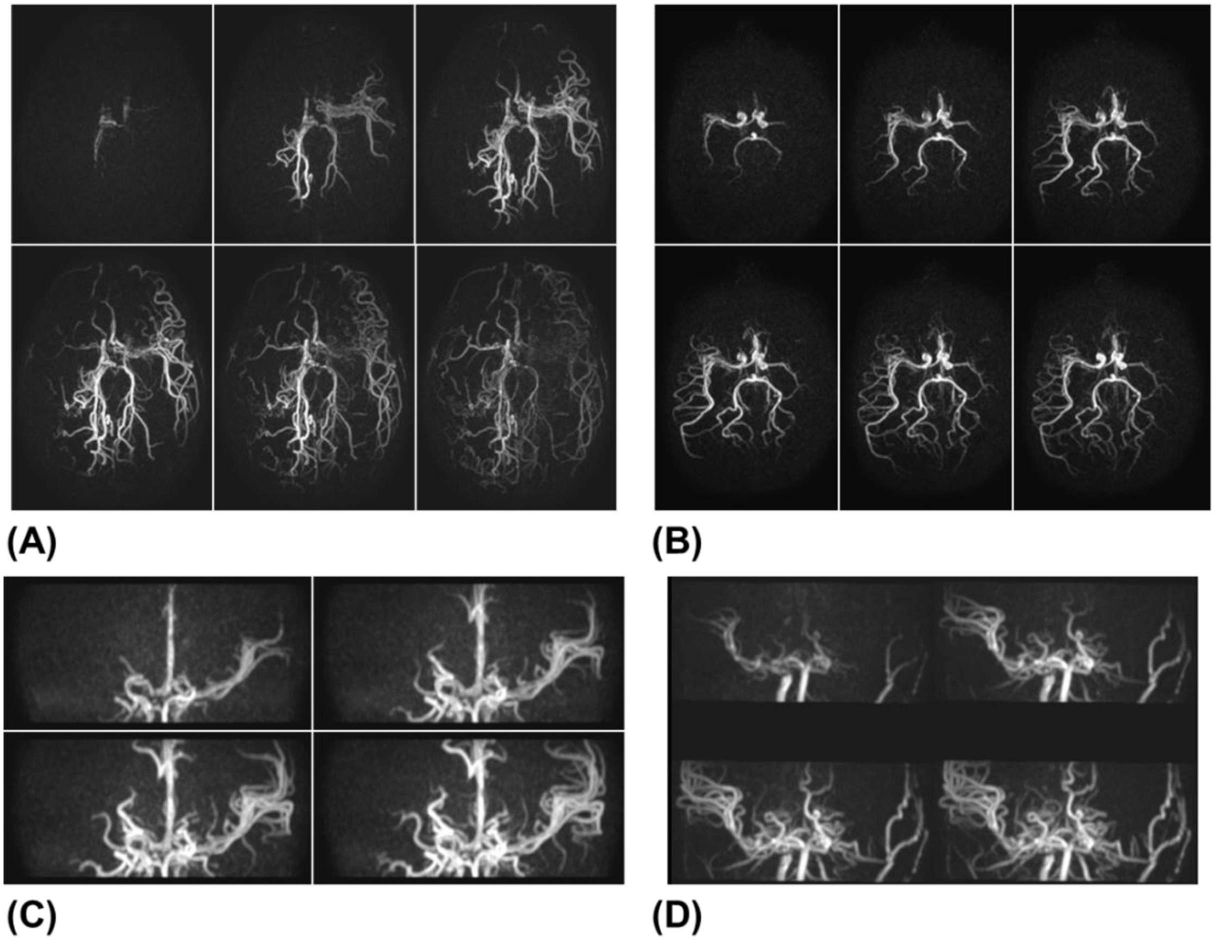

FIGURE 3. Examples of non–gadolinium contrast multidelay arterial spin labeling magnetic resonance imaging of the intracranial vasculature in (A) 13-year-old, (B) eight-month-old, (C) 13-month-old, and (D) seven-year-old patients with moyamoya disease. The first six axial projections are shown in (A, B), whereas the first four coronal projections are shown in (C, D), highlighting the near-submillimeter isotropic resolution of the acquired data. The delay timing of the first frame is 200 ms, followed by 120-ms increments. Note clear demonstration of various degrees of asymmetric vascular filling in all patients. All data were acquired on a 3T Philips Ingenia MRI system. Images courtesy of Masami Yoneyama, Niccolo Stefani, and Jonathan M. Chia (Philips Healthcare), and Amber L. Pokorney and Jeffrey H. Miller (Phoenix Children's Hospital).

spin echo acquisitions that utilize various contrast-generating mechanisms[75] to maximize nerve to soft tissue and signal contrast.[75] Two-dimensional techniques are usually preferred as they can provide high submillimeter in-plane resolution, albeit with thicker slices, whereas three-dimensional methods provide isotropic resolution imaging that can be reformatted in any arbitrary plane for postprocessing visualization.[76] Conventional morphologic imaging methods, such as T1-weighted imaging and fat-suppressed T2-weighted MR neurography, are frequently used for the evaluation of neural pathology, such as changes in signal intensity, course, shape and size, and fascicular pattern, and the detection of fibrosis or mass lesions.[70] Moreover, quantitative methods such as diffusion-weighted imaging and diffusion tensor imaging of the peripheral nerves are becoming popular for more precise assessments of neuropathy.[77-79] Diffusion MR neurography provides the capability to noninvasively characterize nerve fiber microstructure.[80,81]

Regardless of the employed imaging method and the desired T1- or T2-weighted signal contrast, MR neurography applications demand several requirements to produce diagnostic-quality images. First, high nerve-to-surrounding tissue (i.e., muscle) signal contrast and uniform fat suppression are needed. Fat suppression is typically achieved with frequency-selective techniques,[82,83] Dixon-based water-fat separation,[84] or gradient-reversal off-resonance approaches.[85] Second, in addition to fat suppression, MR neurography typically requires additional suppression of signals from adjacent blood vessels and nearby fluids such as cerebral spinal fluid and lymphatics. These can be achieved with a variety of motion-sensitizing methods and manipulations of the turbo spin echo readout scheme.[82-84,86-91] Third, high spatial resolution is a critical requisite for MR neurography due to the inherent small anatomical size of peripheral nerves.[92] The desired spatial resolution must be balanced in the fast or turbo spin echo pulse sequence with adequate SNR ratio, specific absorption ratio limits to prevent excessive tissue heating and maintain patient safety, and total scan duration. Therefore MR neurography in newborns, infants, and small children remain clinically challenging. Figures 4-6 illustrate representative examples of brachial plexus and lumbar plexus MR neurography. Three-dimensional submillimeter-resolution imaging of the brachial plexus typically takes five to seven minutes, whereas a similar scan in the lumbar region takes approximately four to five minutes to complete. Sedation and general anesthesia are not required for MR neurography. However, three-dimensional scans, especially in younger patients, are prone to physiologic and bulk motion artifacts.

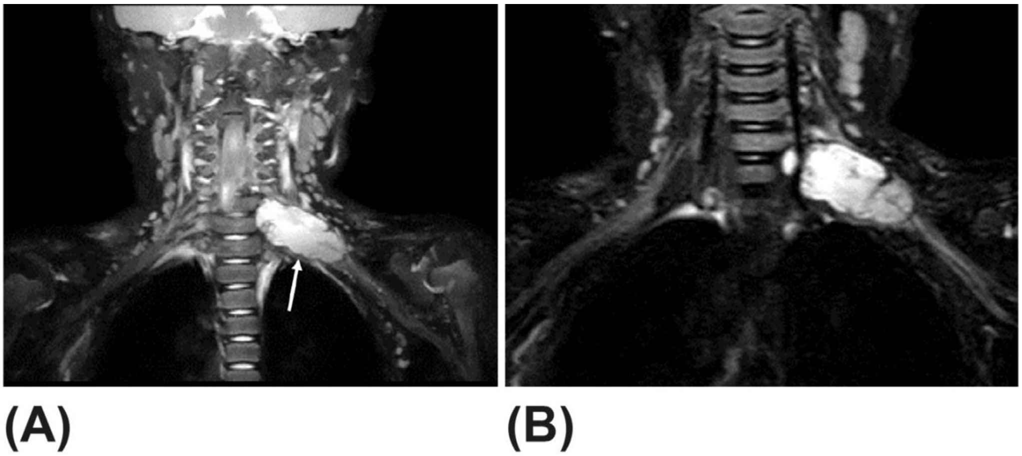

FIGURE 4. (A) A 14-mm maximum intensity projection depicting the brachial plexus of a five-year-old girl with a cervical spinal or brachial plexus tumor (arrow). The tumor is approximately 2 × 4 cm in size and extends laterally through the left C6 and C7 neural foramen. The image was acquired with three-dimensional turbo spin echo sequence combined with two-point Dixon. (B) An individual 1-mm slice through the tumor shown in (A) clearly depicts the cervical nerves affected by the tumor.

Amide proton transfer magnetic resonance imaging

In conventional MRI, the source of the observed signal is hydrogen atoms in "free" water in tissue. In APT MRI, a form of magnetization transfer imaging, also commonly known as *chemical exchange saturation transfer*, the measured signals continue to arise from water protons. However, they have undergone interactions with local amide protons in peptides and macromolecular proteins, such that the signal contrast in APT imaging indirectly reflects the quantity or concentration of endogenous proteins and polypeptide chains in local tissues.[93] In addition to proton magnetization transfer, the APT signal is further dependent on T1 relaxation, the efficiency of water signal saturation by radiofrequency pulses in the APT pulse sequence, and the asymmetry of the magnetization transfer or Z-spectrum, which are described in detail by Xu et al.[94]

Although preclinical animal and clinical human studies involving APT MRI are still in development, the technique has already shown promising diagnostic value in a variety of applications, including brain development, pH monitoring of brain tissues, and the characterization and grading of brain tumors.[95] As a complementary technique, APT MRI has been shown to add diagnostic value when it is coupled with the aforementioned ASL perfusion methods in a comprehensive imaging protocol.[96-98] Beyond the brain, APT MRI has been demonstrated in animal models of lung cancer.[99] Nonetheless, the application of APT MRI in pediatric patients remains limited.

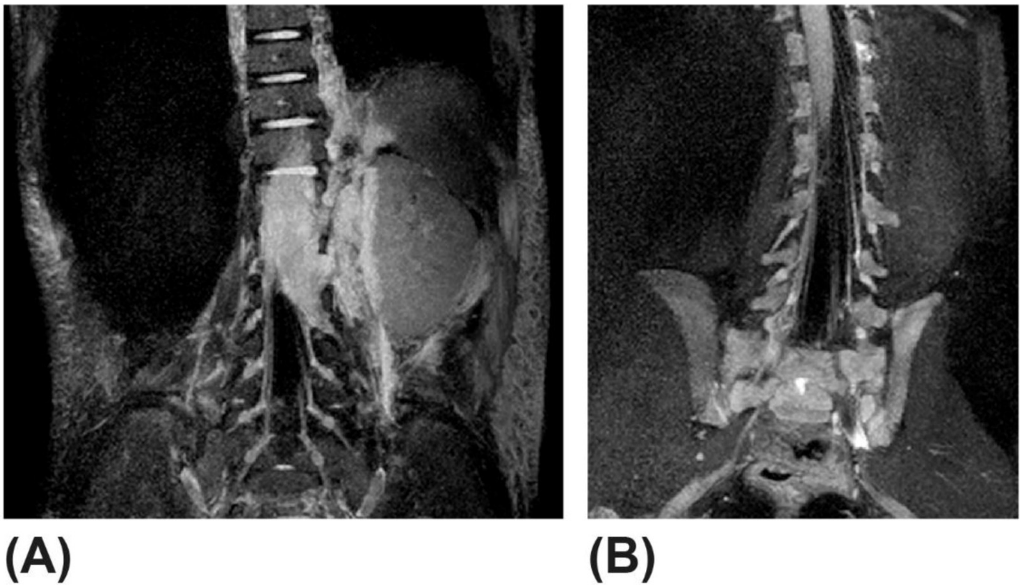

FIGURE 5. (A) A 9-mm maximum intensity projection depicting the lumbar plexus of a two-year-old boy after surgery with previously seen large intra- and extradural masses. The residual intradural component is located mainly in the anterior aspect of the thecal sac and measures approximately 67 × 22 × 10 mm, the left paraspinal component is irregular and measures approximately 39 × 8 mm at the level of L2-L3. There is mild persistent mass effect upon the cord more prominent at the level of L1-L2. The distal spinal canal is again expanded by the tumor, and there is associated scalloping of the posterior vertebral bodies. The image was acquired with fat- and vessel-suppressed 3D TSE. (B) A 9-mm maximum intensity projection depicting the lumbar plexus of a 21-month-old female with severe dextrocurvature of the cervicothoracic junction, apex approximately T1-T2. Mild levocurvature at the thoracolumbar junction. Segmentation anomalies are noted as follows, using S1 as reference: left T6-T7 hemivertebra, T5-T6 incomplete segmentation; right T3-T4 hemivertebra, incomplete segmentation of C2, C3, C4, C5, C6, and C7 with associated butterfly vertebrae. The image was acquired with fat- and vessel-suppressed 3D turbo spin echo sequence.

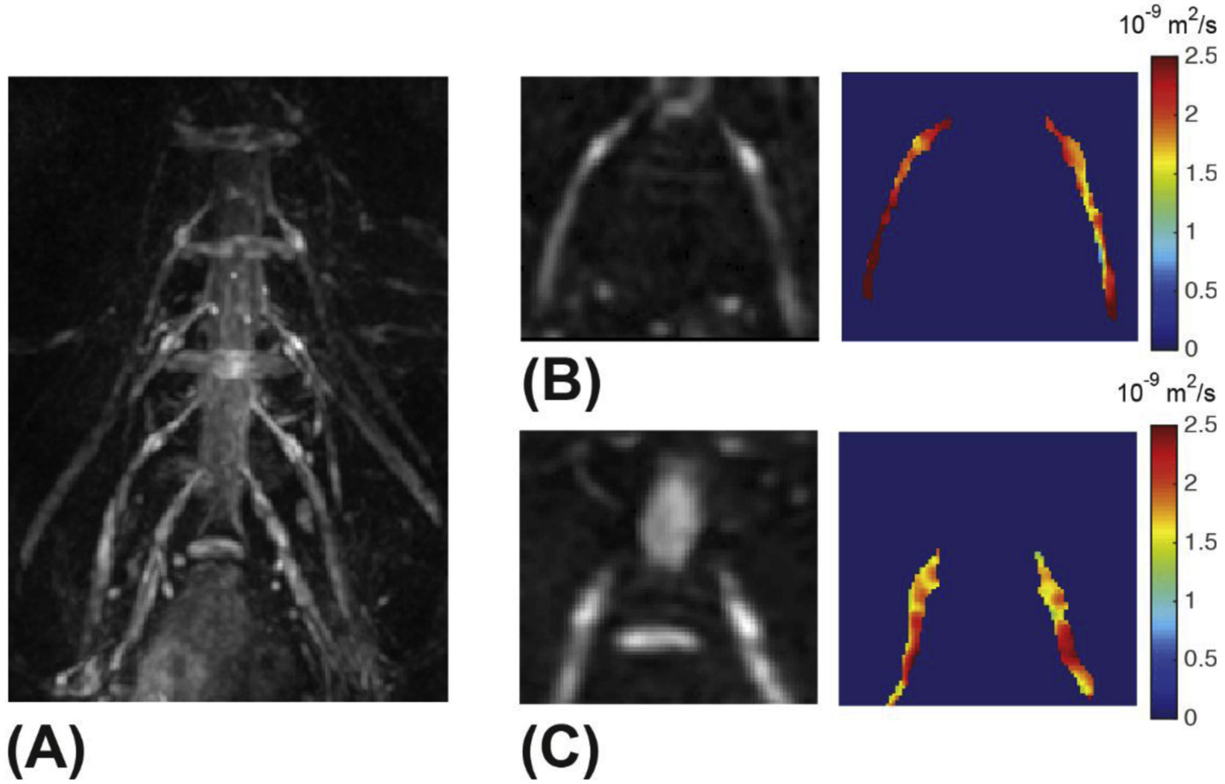

FIGURE 6. (A) Iso-diffusion-weighted image (iso-DWI) depicting the lumbar plexus of a healthy adult acquired with diffusion-prepared three-dimensional turbo spin echo sequence with diffusion acquisitions in six directions using a maximum b-value of 400 s/mm^2. (B) Zoomed-in image of a single-slice iso-DWI depicting the L5 nerves and corresponding mean diffusivity map. (C) Zoomed-in image of a single-slice iso-DWI depicting the S1 nerves and corresponding mean diffusivity map. The color version of this figure is available in the online edition.

In recent studies by Bai et al. and Togao et al., the investigators demonstrated in adult patients with pathology-proven gliomas that APT MRI signals were statistically different between the World Health Organization grade 2, 3, and 4 lesions. The APT signals also correlated more strongly with Ki-67 immunohistochemistry results than with conventional diffusion and perfusion MRI data.[100-102] A plethora of recent studies in humans has further supported the diagnostic utility of APT MRI in preoperative assessment of gliomas and in guiding stereotactic biopsy.[103,104] Togao et al. has additionally shown that quantitative parameters derived from APT MRI have good interscan reproducibility in human trials.[105] Wang et al. has demonstrated that APT and CBF measurements in high-grade gliomas were statistically higher than those in low-grade gliomas in a study of 23 adult patients. In other recent works, APT MRI was demonstrated to be complementary to conventional susceptibility-weighted imaging in detecting acute and subacute intracranial hemorrhage.[106,107] APT MRI has also been demonstrated to successfully differentiate benign and malignant meningiomas.[108] Beyond brain tumors, APT MRI has also been shown to be sensitive to changes in cerebral intracellular pH[109,110] and has been used to identify patients at risk of ischemic stroke.[111,112]

Furthermore, APT MRI has been used to investigate the natural progression of brain development and maturation in neonates and children. In a recent report by Zheng et al.,[113] in 38 neonates, it was reported that APT measurements in the white matter of the frontal lobes, basal ganglia, and occipital lobes were significantly different and that the APT signal positively correlated with gestational age. In a separate study by Zhang et al., in 82 children between the ages two and 190 months, APT signals in the white matter of the corpus callosum, the frontal and occipital lobes, and the centrum semiovale followed an exponentially decreasing curve with age, with the most significant change occurring within the first year of life.[114] Preliminary studies describing APT in children with developmental delays[115] and in elderly patients with Alzheimer disease have also been reported.[116]

As advances in MRI hardware and pulse sequence capabilities continue to emerge and improve, APT imaging is now possible in the clinical setting with several vendors offering the technique and its related postprocessing computations as a work-in-progress package. One of the main attractions of APT imaging in brain tumor characterization is its lack of requirement for intravenous gadolinium contrast agents, as the technique solely relies on the endogenous signal contrast of water protons and their interactions with neighboring amide protons. In human brain imaging, typical APT scan times for whole-brain coverage on a 3-T MRI platform range from five to seven minutes, depending on the extent of the pathology. Two examples are shown in Figs 7 and 8. The APT acquisition itself is also not dependent on sedation or general anesthesia and can be performed in awake patients. However, due to the relatively long scan times, head motion should be minimized.

Neuromuscular imaging

Moving through the body from ASL and APT methods in brain imaging to MR neurography in spine and peripheral nerve applications, the review now shifts attention to inform the reader briefly of some of the advanced MR methods in neuromuscular imaging that is current available to clinicians and researchers. This section is written concisely for the practicing neurologist to familiarize him or her with new imaging terminology in neuromuscular disease.

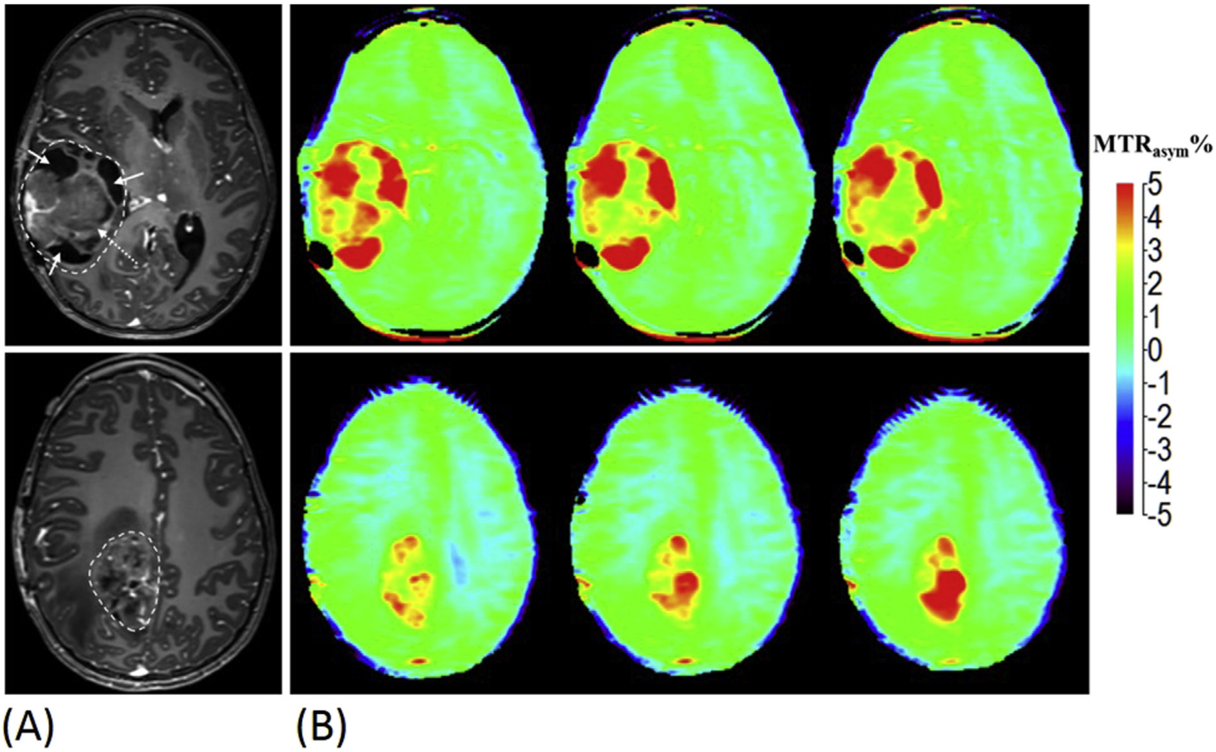

FIGURE 7. Examples of amide proton transfer (APT) magnetic resonance imaging in an 11-year-old with two intra-axial masses of metastatic Ewing sarcoma (white dashed outlines), one in the right temporal lobe (top row) and the other in the right parietal lobe (bottom row). Post-gadolinium contrast-enhanced T1-weighted anatomical images are shown in (A). Three consecutive APT-sourced magnetization transfer ratio (MTR) images are shown in (B). The −5% to +5% color scale is shown using the literature standard convention for MTR. Note that multiple cysts in the temporal lobe mass (solid arrows) are characterized by strong MTR signal, suggesting higher proteinaceous content than solid components of the mass (dotted arrow). Note also subtle differences in MTR ratio between white and gray matter in (B). All data were acquired on a 3T Philips Ingenia MRI system. Images courtesy of Jochen Keupp and Jonathan M. Chia (Philips HealthTech) and John Curran (Phoenix Children's Hospital). The color version of this figure is available in the online edition.

The interested reader is referred to the extensive bibliography for further reading.

The typical management of a patient with suspected neuromuscular disease involves the examination of clinical history and various types of functional and neurological tests such as the six-minute walk test and manual muscle testing to assess mobility and muscle strength.[117] In many instances, muscle biopsies are also obtained as part of the routine clinical evaluation.[118,119] Neuromuscular imaging with MRI and MR spectroscopy of the upper limbs and lower extremities has become widely popular in large clinical centers conducting therapeutic trials as an additional and complementary diagnostic tool.[120] Noninvasive imaging provides qualitative and quantitative correlates to functional tests, biopsies, and electrodiagnostic results.[121] In addition, MRI characterizes the involvement of muscular dystrophy disease across different muscles and highlights the degree and disease-specific patterns of muscle involvement.[122-126]

T1-weighted imaging has been the workhorse pulse sequence to qualitatively assess muscle fat infiltration patterns.[127] Likewise, complementary short tau inversion recovery T2-weighted imaging has been used to assess muscle edema and fibrosis patterns.[128] Both T1- and T2-weighted imaging features have been characterized semiquantitatively with scalar ratings. For example, the four-point Mercuri scale is commonly used to categorize the fatty infiltration of muscle tissue starting from 0% (score 1) to above 60% (score 4) on axial T1-weighted images.[129] Similarly, an intramuscular T2 hyperintense signal indicating muscle edema can be assessed with a multi-point rating scale, as suggested by Morrow et al.[130]

Beyond conventional T1- and T2-weighted imaging, quantitative MR methods including fat fraction MRI, T1 mapping,[131] T2 mapping, and relatedly multiecho proton spectroscopy have emerged over the past decade as standardized and popular outcome measures in neuromuscular imaging.[132] These accurate and precise imaging biomarkers are frequently utilized in clinical trials of neuromuscular disease involving gene therapy and pharmacogenetics.[133-136] Quantitative imaging biomarkers like fat fraction and T2 mapping have significant advantages over qualitative T1- and T2-weighted imaging in longitudinal studies aimed at evaluating therapy efficacy. Namely, they are repeatable and reproducible on several scales, including minimal variations within a subject from one examination to another, and more importantly from one MRI platform to another (e.g., different magnetic field strength or different equipment vendor), and possibly across separate institutions. In addition, they are particularly useful in objectively differentiating patient and healthy control groups.[137,138] It is worth noting that many of these aforementioned imaging techniques are not unique to skeletal muscle characterization, and their usage can be extended to multiple anatomies, tissues, and organs, including most notably bone marrow assessment,[139-141] myocardial characterization,[142,143] and liver.[144,145]

Developed originally for hepatic fat content quantification, the proton density (PD) fat fraction metric derived from chemical-shift-encoded multiecho MRI has emerged as a robust quantitative imaging biomarker for a wide range of fat-containing tissues,[139,146-148] including skeletal muscles[149] As shown in Fig 9, the technique provides on a voxel-by-voxel basis the percent fat content within each muscle region. Fat fraction mapping has been shown to reliably track disease progression[120] and also as a strong correlate to functional examinations.[150,151] The use of fat fraction mapping to determine the spatial pattern of fat infiltration across different muscles and within one muscle for different diseases remains an active area of research.[152]

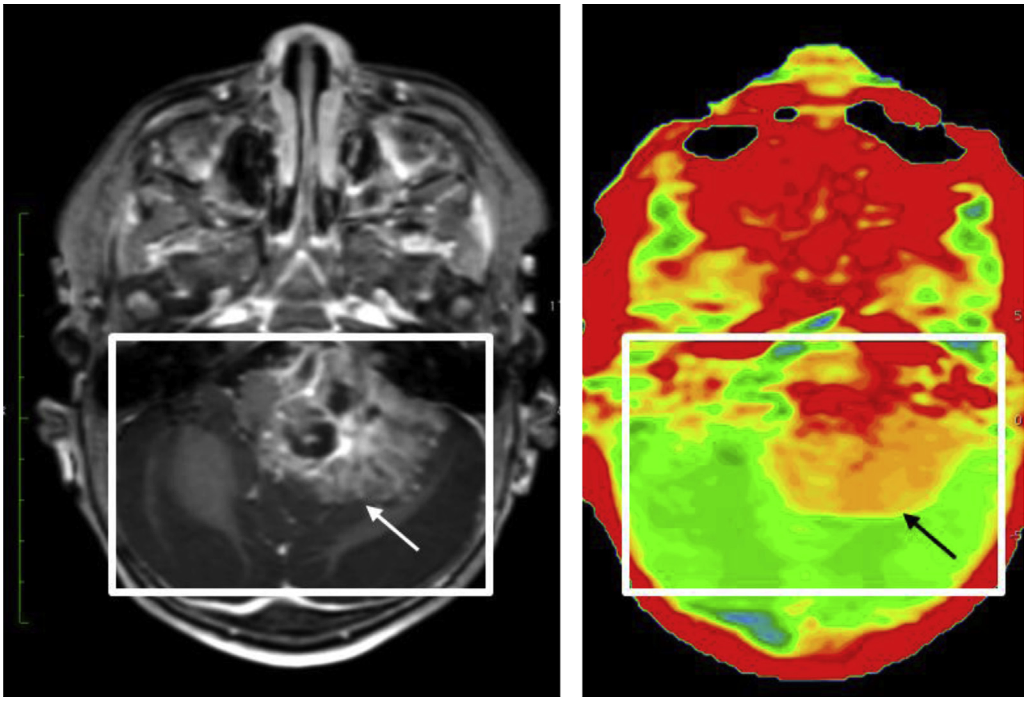

FIGURE 8. Magnetic resonance imaging in a 4-month-old female with a large posterior fossa mass (arrow), which is clearly seen on the amide proton transfer (APT) image (right). Example shows the sensitivity of the APT technique to B0 magnetic field homogeneity. White box outlines the shim area within which magnetic field homogeneity is optimized for uniformity. Note that the APT signal outside of the shim box is saturated and erroneous, especially around the orbits. Same APT color scale as Figure 7. Images courtesy of Jochen Keupp and Jonathan M. Chia (Philips HealthTech) and John Curran (Phoenix Children's Hospital). The color version of this figure is available in the online edition.

Similarly, T2 mapping[153-155] of skeletal muscles has been used in neuromuscular disease characterization of tissue edema and fibrosis.[133,153] In diseased patients, the T2 of affected muscle is typically greater than that of normal and healthy muscle. Muscle T2 values are also computed on a voxel-by-voxel basis using multiecho spin-echo-based pulse sequences, and regional averages in various

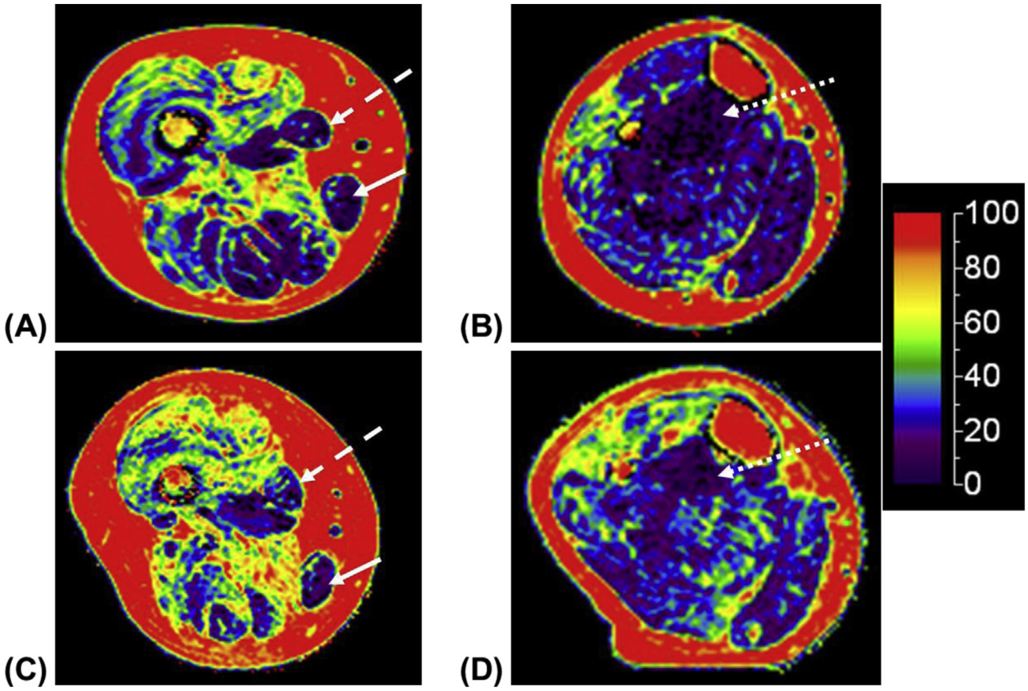

FIGURE 9. Proton density fat fraction (PDFF) images from Dixon water-fat magnetic resonance imaging (MRI) of a nine-year-old boy with Duchenne muscular dystrophy. Axial images of the upper (A, C) and lower (B, D) leg extremities are shown on a color scale representing 0% to 100% fat fraction. These images illustrate increasing fat content in various muscle groups across a time span of four months, from (A, B) September 2012 to (C, D) January 2013. Note interestingly that certain muscles do not demonstrate a significant increase in fat content, such as the gracilis (solid arrow), adductor longus (dashed arrow), and posterior tibialis (dotted arrow). Data acquired on a 3T Philips Achieva MRI system. Images courtesy of Skorn Ponrartana, MD, PhD and Tishya Wren, PhD (Children's Hospital Los Angeles). The color version of this figure is available in the online edition.

muscles have been used to compare patients and healthy control groups as well as track disease progression in response to therapeutic intervention.[156,157] Using both fat fraction and T2 mapping, Carlier et al. showed in adult patients with Pompe disease that fat infiltration progresses faster in muscles with elevated water T2.[158] Figure 10 illustrates an example in an adult patient. Last, single-voxel multiecho MR spectroscopy is typically performed in one muscle group at a time to jointly estimate fat fraction (and T2 values) as well as estimate the degree of triglyceride unsaturation by highlighting the olefinic resonance.[159] Complementary imaging techniques have also been developed for simultaneous T2 and fat fraction mapping.[132,160] T2 mapping has also been used in the assessment of skeletal muscle replacement by connective tissues composed primarily of collagen, which leads to fibrosis. More recently, ultrashort echo time (TE) MRI has been proposed for assessing the short T2 components (i.e., collagen, cortical bone, fascia) in muscles undergoing fibrotic changes.[161] Both fat fraction and T2 mapping of the lower extremity or upper limb usually takes three to five minutes per patient side, depending on the acquired spatial resolution and three-dimensional volume coverage. Sedation and general anesthesia are again not strictly required for these methods. However, patient cooperation to keep the imaging area of interest relatively motionless is required. As discussed in the second portion of the review, compressed sensing has been successfully used to accelerate data acquisition speed in muscular dystrophy studies.[162,163]

Recent advances in accelerated MRI data acquisition methods

The first part of this review focused primarily on newly developed mechanisms to generate signal contrast in MRI and their associated applications; the second part will describe new data acquisition strategies aimed to accelerated MRI data acquisition speed and reduce scan time. In contrast to other radiologic imaging modalities, most notably computed tomography and ultrasound, data acquisition speed in MRI is slow. Each scan in an MRI protocol often requires several minutes to complete, especially when three-dimensional volumetric coverage is required. The principal reason for this limitation is that MRI data are acquired in the alternate spatial frequency domain, often referred to as the k-space,[164-166] A full discussion of k-space is beyond the scope of this review. However, the interested reader is referred to several excellent pictorial descriptions of k-space, written for the clinician. To generate a series of images, it typically takes thousands to tens of thousands of repetitions of an MRI pulse sequence to adequately fill k-space and represent with good fidelity the object or anatomy of interest. Many of the following data acquisition techniques can be combined with the aforementioned imaging methods from the prior section, and the description of these integrations will be alluded to at the conclusion of this review.

Over the past two decades, the advent of multielement receiver coil arrays and parallel imaging technology[167,168] revolutionized accelerated MRI data acquisition. Parallel imaging is now ubiquitous and used across nearly all clinical MRI protocols. In the following section, we briefly review three emerging accelerated data acquisition methods that have garnered increasing interest and development in the MRI community. These methods[163] include simultaneous multislice or multiband imaging, compressed sensing MRI,[169] and synthetic MRI and MR fingerprinting.[170] Clinical examples in pediatric patients accompany each technique. Each of these three techniques is further compatible with existing parallel imaging methods and with each other to provide even higher cumulative acceleration rates. These techniques are continuously being explored in research and potential clinical applications.[171-173] Table 2 shows the applications, benefits, and potential limitations of these techniques.

Simultaneous multislice MRI

Simultaneous multislice imaging[174] is an increasingly popular technology that allows the radiofrequency excitation, selection, and acquisition of several parallel slices at the same time. This method is also commonly referred to as *multiband MRI*. In contrast to conventional MRI methods wherein data from only one slice is selected and acquired at any given instance, simultaneous multislice (SMS) imaging with an acceleration factor of 2 to 4 has been successfully demonstrated in brain imaging.[175-179]

The process of SMS imaging is shown in Fig 11. The initial raw data lead to a superposition of information from the multiple slice locations. In Fig 11, an acceleration factor of 2 is illustrated. As all modern scanners have multichannel head coils that surround the patient, these arrays impart varying coil sensitivity information on the superimposed SMS data, and knowledge of these coil sensitivities facilitates the subsequent separation of the superimposed slices. The superimposed slices can further be shifted with respect to one another to improve the separation process by maximizing overlap with background areas. Since its initial description 2013 by Feinberg and Setsompop et al.,[177,180] SMS has gained widespread popularity in neuroscience research involving resting and task-based functional MRI[181,182] and diffusion tractography imaging to accelerate the scan time of these long acquisitions.[177,183-185] SMS-based protocols have become the foundation of MRI sequences used in the Human Connectome Project, accelerating both functional MRI and diffusion tractography imaging data acquisition speed by factors of two to four.[186]

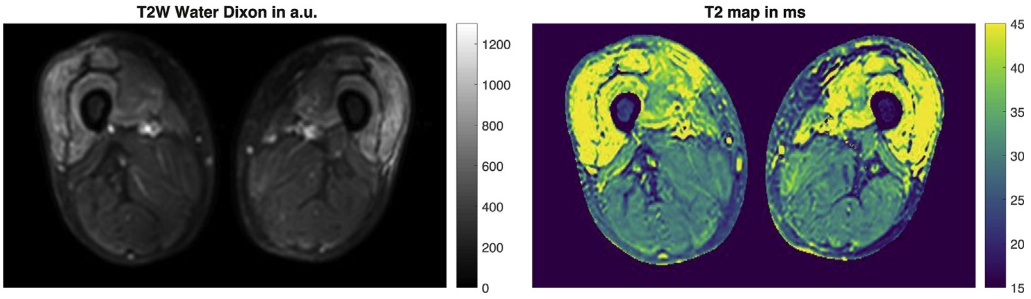

FIGURE 10. T2-weighted Dixon water image of the thigh musculature of a 41-year-old male patient with myositis (left) and the corresponding T2 map acquired with a T2-prepared 3D turbo spin echo sequence (right). Both the qualitative Dixon water image and the quantitative T2 map show the same pattern for T2 elevations in the quadriceps muscles, whereas the quantitative T2 mapping technique allows a more objective analysis of the thigh musculature. Images courtesy of Dominik Weidlich and Sarah Schlaeger (Technical University of Munich). The color version of this figure is available in the online edition.

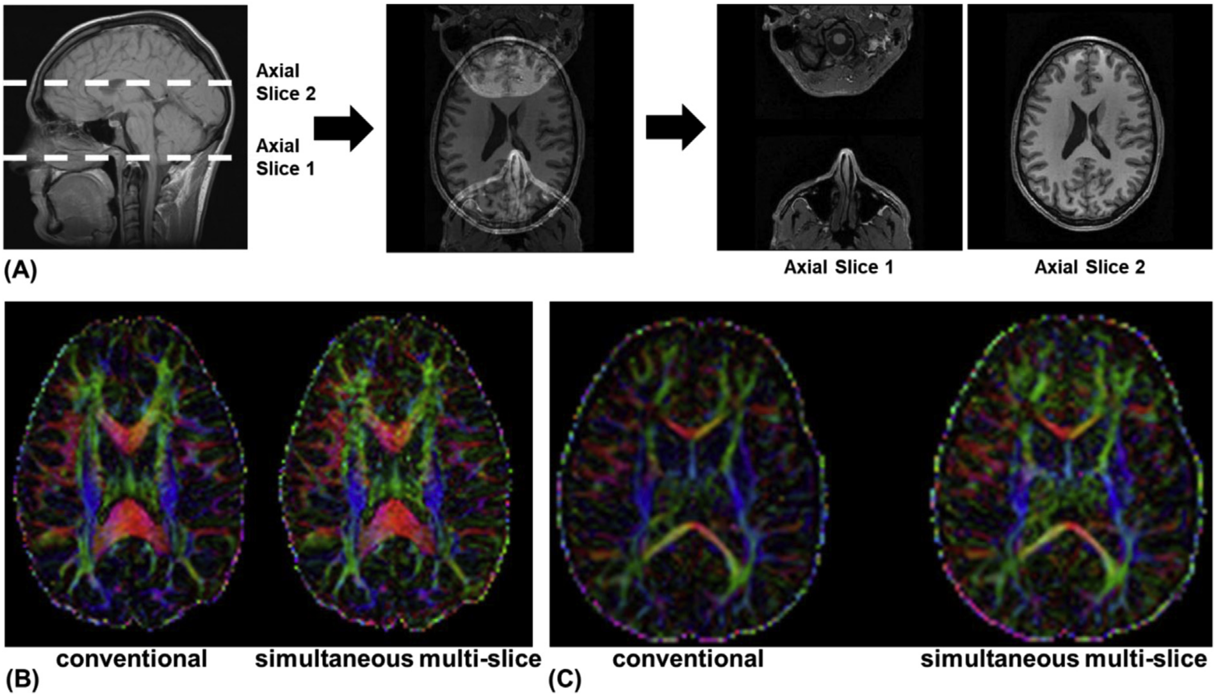

FIGURE 11. (A) Pictorial illustration of simultaneous multislice magnetic resonance imaging (MRI). Unlike conventional MRI, in which data from a single slice is acquired at a time, simultaneous multislice MRI acquires multiple slices per radiofrequency excitation, where each of the excited slices are offset by a spatial shift. The raw image contains overlapping signals from both slices. The slice-specific signals are separated out in postprocessing using parallel-imaging algorithms. (B) and (C) Examples of 64- and 128-directional fractional anisotropy maps; MRI data in a 10-year-old and a three-month-old patient, respectively. In each image pair, the simultaneous multislice acquisition, which is twofold faster in scan time, is shown on the right. The technology thus allows 64- and 128-direction diffusion tensor imaging data to be collected in five to seven minutes. All data were acquired on a 3T Philips Ingenia MRI system. Images courtesy of Jonathan M. Chia (Philips HealthTech) and Amber L. Pokorney and Jeffrey H. Miller (Phoenix Children's Hospital). The color version of this figure is available in the online edition.

Compressed sensing

Similar to parallel imaging techniques, a fundamental principle underlying compressed sensing MRI is the approach to acquire k-space data in an undersampled fashion.[187-192] Parallel imaging uniformly undersamples k-space leading to structured aliasing artifacts in the resultant image. Compressed sensing undersampling is nonuniform. The resulting artifacts are incoherent and often

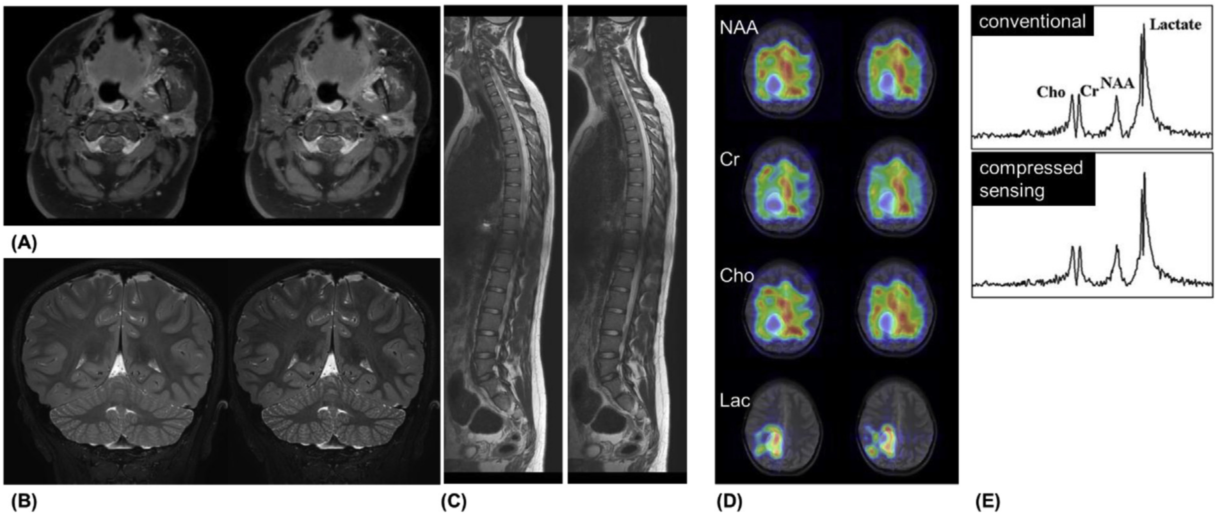

FIGURE 12. Examples of compressed sensing magnetic resonance imaging in the brain and spine, shown for (A) axial post-gadolinium contrast-enhanced fat-suppressed T1-weighted turbo spin echo data, (B) coronal T2-weighted turbo spin echo data, (C) sagittal non–fat-suppressed T2-weighted turbo spin echo, and (D) two-dimensional multi-voxel spectroscopy of metabolites *N*-acetyl-L-aspartate (NAA), creatine (Cr), choline (Cho), and lactate (Lac). In each image pair, the conventional data acquisition is shown on the left, and the compressed sensing-acquired image is shown on the right, representing an approximate 45% reduction (A–C) in scan time without compromising spatial resolution and diagnostic image quality. In (D), a threefold reduction in scan time is demonstrated with compressed sensing. (E) One-dimensional spectrum of a voxel in the Ewing sarcoma, comparing (top) conventional and (bottom) compressed sensing results. The color representation is relative metabolite concentration from low (blue) to high (red). All data were acquired on a 3T Philips Ingenia MRI system. (A–C) Images courtesy of Jonathan M. Chia (Philips HealthTech) and Amber L. Pokorney and Jeffrey H. Miller (Phoenix Children's Hospital). (D) Images courtesy of Rohini Vidya Shankar and Vikram Kodibagkar (Arizona State University). The color version of this figure is available in the online edition.

blurred making them less noticeable to the human eye. Another fundamental principle of compressed sensing is a representation of the desired image in a sparse k-space domain, where image reconstruction from highly undersampled k-space data is feasible. In the case of MR angiography,[193] the underlying structures are inherently sparse in the spatial image domain (i.e., vessel pixels are bright, whereas background pixels are dark). In situations where the image is not sparse in the image domain, a transform such as the wavelet transform, often used in JPEG compression, is applied. MRI data can also be sparse in the temporal domain, for example, in the form of a beating heart. If the heart rate is a constant 60 beats per minute, the sparse representation of such periodic motion is simply 1 Hz in the frequency domain.[189] Figure 12 provides examples of compressed sensing MRI in pediatric brain and spinal MRI.

MR fingerprinting and synthetic MRI

Synthetic MRI[194-200] and magnetic resonance fingerprinting[170,201-206] are revolutionary new techniques that break away from existing MRI principles of data acquisition. In conventional MRI, pulse sequences acquire a given tissue contrast (i.e., relative T1-weighted, relative T2-weighted, PD, apparent diffusion coefficients, etc.) with a specified set of pulse sequence timing parameters (i.e., repetition time [TR], TE, inversion time, flip angle, spatial resolution, signal bandwidth). In the resultant image, the voxel values (i.e., signal intensities) are relative, and the true PD and T1 and T2 relaxation times of the underlying tissue remain unknown. If a new image is desired with different tissue signal contrast, a separate pulse sequence must be performed after selecting different timing values, at the expense of additional scan time.

Synthetic MRI and MR fingerprinting are at their core foundation parameter mapping techniques that aim to quantify the fundamental T1, T2, and PD constants of the underlying anatomy on a voxel-wise basis. MR fingerprinting employs an acquisition with varying values of sequence parameters in a time series loop. The subsequent output of the acquisition is in essence a signal fingerprint, a unique signal profile for a given set of T1, T2, and PD constants. By acquiring a "fingerprint" for each voxel and matching

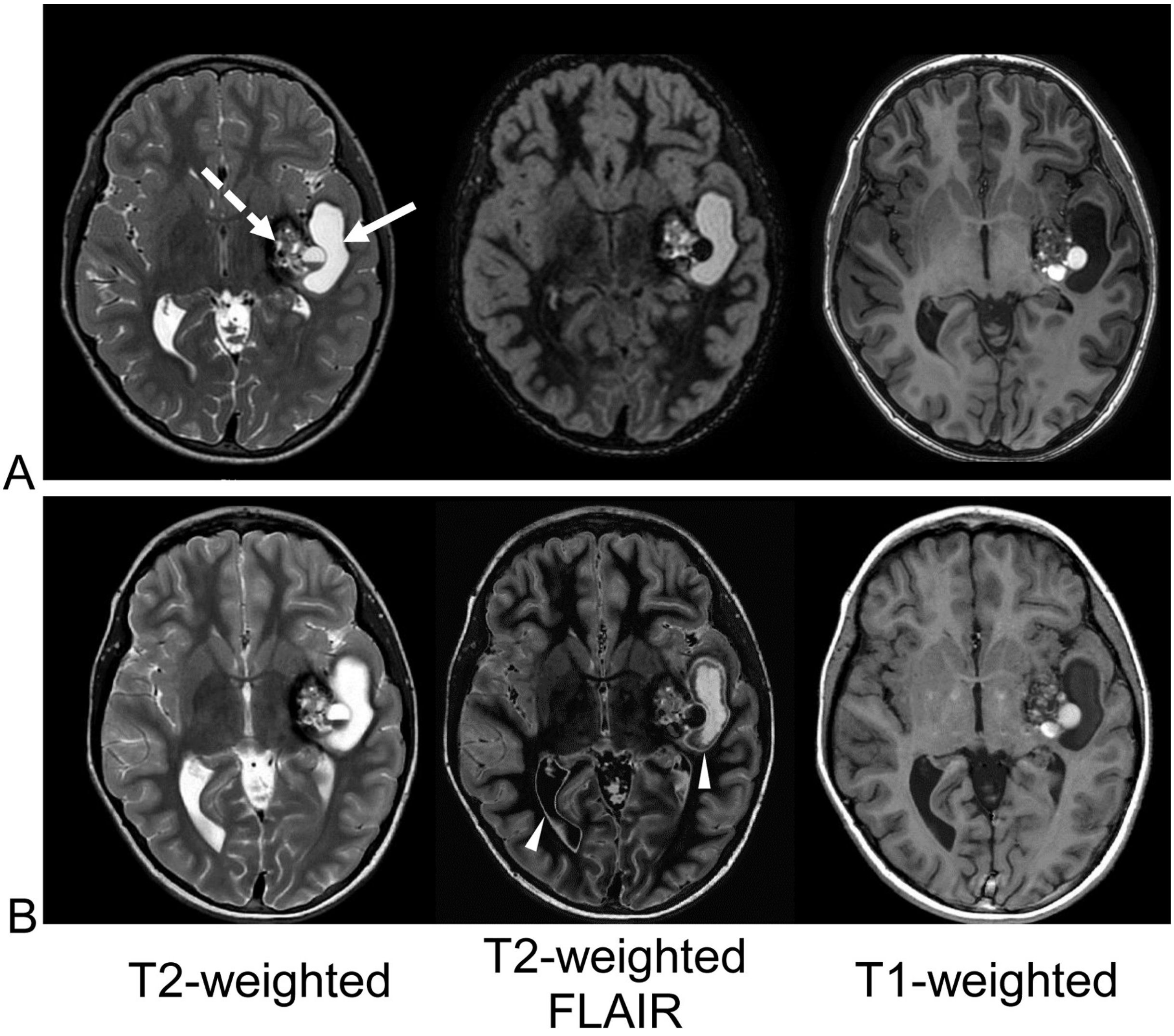

FIGURE 13. Exemplary images from synthetic magnetic resonance imaging (GE Healthcare's MAGiC pulse sequence, scan time five minutes 30 seconds) demonstrating a cavernous hemangioma (dotted arrow) and a cyst (solid arrow) in an eight-year-old boy. (A) Conventional images and (B) MAGiC data. Differences between the two acquisitions are mostly evident in the second column of T2-weighted fluid attenuated inversion recovery images, where the MAGiC data show artifacts arising from partial volume effects at the boundary between cerebrospinal fluid (CSF) and brain tissues (arrowheads). These are well-known artifacts in MAGiC and arise from the large difference in T1 and T2 values between pure CSF and brain tissues, which lead to an erroneous curve fitting of the signal in these boundary voxels. Images courtesy of Liz Ivarsson (Queen Silvia Children's Hospital, Gothenberg, Sweden).

them to a pre-established "dictionary" or database of known profiles that accounts for all possible combinations, the desired T1, T2, and PD values are revealed. In contrast then to conventional MRI methods, MR fingerprinting yields direct quantitative estimates of tissue properties of interest via a single scan. Once these properties are extracted on a voxel-wise basis, one can conceivably *synthesize* any resultant data set of the patient's imaging volume with arbitrary tissue contrast weightings and pulse sequence timing parameters. Similar to MR fingerprinting, synthetic MRI measures quantitative T1, T2, and PD values of each voxel in the imaged volume utilizing a single sequence with multiple saturation time delays and TEs. The acquired data for each voxel are then fitted to the Bloch equations governing MRI physics to yield T1, T2, and PD values.[207] Recent literature has compared the diagnostic equivalence of synthetic MRI data with those that are acquired by conventional sequences.[199,200] Multiple diagnostic sequences can therefore be replaced with a single acquisition theoretically decreasing the time necessary for an imaging session. Figure 13 illustrates an example.

Apart from the flexibility of synthetic image generation, direct measurement of quantitative T1, T2, and PD values can be utilized for other purposes. For example, automated tissue segmentation of gray and white matter and CSF has been demonstrated,[208] as well as myelin volumes and myelin fraction estimation.[209] These assessments make minimal assumptions of the underlying anatomy and do not require a normative database, such as the MNI and Talairach atlases. The normal growth trajectories of intracranial volume, gray and white matter volumes, and myelin volume in children aged zero to 20 years using synthetic MRI has been reported.[195] With both MR fingerprinting and synthetic MRI, the direct estimation of quantitative image biomarkers such as T1, T2, and PD can potentially lead to new approaches for assessing diseases and their progression.

Conclusion

We have summarized some of the recent advances in brain, spine, and neuromuscular imaging, with a particular focus on pediatric applications. Methods like ASL and APT MRI, respectively, have the potential to complement or potentially replace existing methods for brain perfusion and tumor assessment that require contrast agent administration, as concerns for possible effects of gadolinium-based retention and deposition continue to persist in the literature and MRI community.[210] New developments in three-dimensional submillimeter MR neurography that incorporate fat, cerebrospinal fluid, and blood signal suppression can enable clear delineation of brachial and lumbar plexus nerves[92] and demonstrate strong potential in providing clinical value to the assessment of children who have birth-related injuries,[211] traumatic cervical spine injuries from trauma, genetic disorders such as neurofibromatosis, and cervical spine tumors. In neuromuscular disease imaging, robust and reliable quantitative biomarkers including fat fraction and T2 mapping have enabled repeatable and reproducible assessment of muscle involvement, injury, and response to therapy, facilitating greater clinical trial efforts globally.

For pediatric MRI, reduction in both scan time and the use of sedation and general anesthesia continue to be a strategic goal for the clinical community.[212-215] Novel and innovative data acceleration methods in MRI, including simultaneous multislice acquisition, compressed sensing, and synthetic MRI and MR fingerprinting, along with combinations of these methods,[179] are promising solutions, and more widespread evaluation of these techniques are needed to bring them to the forefront of mainstream MRI practice.

References

1. Branco P, Ayres-Basto M, Portugal P, Ramos I, Seixas D. Brain magnetic resonance imaging: perception and expectations of neurologists, neurosurgeons and psychiatrists. Neuroradiol J. 2014;27:261–267.
2. Koretsky AP. New developments in magnetic resonance imaging of the brain. NeuroRx. 2004;1:155–164.
3. Rocchi L, Niccolini F, Politis M. Recent imaging advances in neurology. J Neurol. 2015;262:2182–2194.
4. Ahmad R, Hu HH, Krishnamurthy R, Krishnamurthy R. Reducing sedation for pediatric body MRI using accelerated and abbreviated imaging protocols. Pediatr Radiol. 2018;48:37–49.
5. Wang X, Xu Z, Miao CH. Current clinical evidence on the effect of general anesthesia on neurodevelopment in children: an updated systematic review with meta-regression. PLoS One. 2014;9:e85760.
6. Ing C, Sun M, Olfson M, et al. Age at exposure to surgery and anesthesia in children and association with mental disorder diagnosis. Anesth Analg. 2017;125:1988–1998.
7. Detre JA, Wang J, Wang Z, Rao H. Arterial spin-labeled perfusion MRI in basic and clinical neuroscience. Curr Opin Neurol. 2009;22:348–355.
8. Lee S, Yun TJ, Yoo RE, et al. Monitoring cerebral perfusion changes after revascularization in patients with moyamoya disease by using arterial spin-labeling MR imaging. Radiology. 2018;288:565–572.
9. Juttukonda MR, Jordan LC, Gindville MC, et al. Cerebral hemodynamics and pseudo-continuous arterial spin labeling considerations in adults with sickle cell anemia. NMR Biomed. 2017;30(2).
10. Carsin-Vu A, Corouge I, Commowick O, et al. Measurement of pediatric regional cerebral blood flow from 6 months to 15 years of age in a clinical population. Eur J Radiol. 2018;101:38–44.
11. Liu F, Duan Y, Peterson BS, et al. Resting state cerebral blood flow with arterial spin labeling MRI in developing human brains. Eur J Paediatr Neurol. 2018;22:642–651.
12. Hoge RD, Pike GB. Oxidative metabolism and the detection of neuronal activation via imaging. J Chem Neuroanat. 2001;22:43–52.
13. Akgoren N, Fabricius M, Lauritzen M. Importance of nitric oxide for local increases of blood flow in rat cerebellar cortex during electrical stimulation. Proc Natl Acad Sci U S A. 1994;91:5903–5907.
14. Ye FQ, Berman KF, Ellmore T, et al. H(2)(15)O PET validation of steady-state arterial spin tagging cerebral blood flow measurements in humans. Magn Reson Med. 2000;44:450–456.
15. Feng CM, Narayana S, Lancaster JL, et al. CBF changes during brain activation: fMRI vs. PET Neuroimage. 2004;22:443–446.
16. Zhang K, Herzog H, Mauler J, et al. Comparison of cerebral blood flow acquired by simultaneous [15O]water positron emission tomography and arterial spin labeling magnetic resonance imaging. J Cereb Blood Flow Metab. 2014;34:1373–1380.
17. Heijtel DF, Mutsaerts HJ, Bakker E, et al. Accuracy and precision of pseudo-continuous arterial spin labeling perfusion during baseline and hypercapnia: a head-to-head comparison with (1)(5)O H(2)O positron emission tomography. NeuroImage. 2014;92:182–192.
18. Cha YH, Jog MA, Kim YC, Chakrapani S, Kraman SM, Wang DJ. Regional correlation between resting state FDG PET and pCASL perfusion MRI. J Cereb Blood Flow Metab. 2013;33:1909–1914.
19. Newberg AB, Wang J, Rao H, et al. Concurrent CBF and CMRGlc changes during human brain activation by combined fMRI-PET scanning. Neuroimage. 2005;28:500–506.
20. Chen Y, Wolk DA, Reddin JS, et al. Voxel-level comparison of arterial spin-labeled perfusion MRI and FDG-PET in Alzheimer disease. Neurology. 2011;77:1977–1985.
21. Wang J, Licht DJ, Jahng GH, et al. Pediatric perfusion imaging using pulsed arterial spin labeling. J Magn Reson Imaging. 2003;18:404–413.
22. Miranda MJ, Olofsson K, Sidaros K. Noninvasive measurements of regional cerebral perfusion in preterm and term neonates by magnetic resonance arterial spin labeling. Pediatr Res. 2006;60:359–363.
23. Biagi L, Abbruzzese A, Bianchi MC, Alsop DC, Del Guerra A, Tosetti M. Age dependence of cerebral perfusion assessed by magnetic resonance continuous arterial spin labeling. J Magn Reson Imaging. 2007;25:696–702.
24. Wang J, Rao H, Detre JA. Arterial spin labeling perfusion MRI in developmental neuroscience. In: Rumsey JM, Ernst M, eds. Neuroimging in Developmental Clinical Neuroscience. Cambridge: Cambridge University Press; 2009:326–343.
25. Chiron C, Raynaud C, Maziere B, et al. Changes in regional cerebral blood flow during brain maturation in children and adolescents. J Nucl Med. 1992;33:696–703.
26. Chugani HT. A critical period of brain development: studies of cerebral glucose utilization with PET. Prev Med. 1998;27:184–188.
27. Taki Y, Hashizume H, Sassa Y, et al. Correlation between gray matter density-adjusted brain perfusion and age using brain MR images of 202 healthy children. Hum Brain Mapp. 2011;32:1973–1985.
28. Taki Y, Hashizume H, Sassa Y, et al. Gender differences in partial-volume corrected brain perfusion using brain MRI in healthy children. NeuroImage. 2011;58:709–715.
29. Satterthwaite TD, Shinohara RT, Wolf DH, et al. Impact of puberty on the evolution of cerebral perfusion during adolescence. Proc Natl Acad Sci U S A. 2014;111:8643–8648.

30. Avants BB, Duda JT, Kilroy E, et al. The pediatric template of brain perfusion. Sci Data. 2015;2:150003.
31. Jain V, Duda J, Avants B, et al. Longitudinal reproducibility and accuracy of pseudo-continuous arterial spin-labeled perfusion MR imaging in typically developing children. Radiology. 2012;263:527–536.
32. Licht DJ, Wang J, Silvestre DW, et al. Preoperative cerebral blood flow is diminished in neonates with severe congenital heart defects. J Thorac Cardiovasc Surg. 2004;128:841–849.
33. Chen J, Licht DJ, Smith SE, et al. Arterial spin labeling perfusion MRI in pediatric arterial ischemic stroke: initial experiences. J Magn Reson Imaging. 2009;29:282–290.
34. Jann K, Hernandez LM, Beck-Pancer D, et al. Altered resting perfusion and functional connectivity of default mode network in youth with autism spectrum disorder. Brain Behav. 2015;5:e00358.
35. Ho TC, Wu J, Shin DD, et al. Altered cerebral perfusion in executive, affective, and motor networks during adolescent depression. J Am Acad Child Adolesc Psychiatry. 2013;52:1076–10791 e2.
36. Schrantee A, Mutsaerts H, Bouziane C, Tamminga H, Bottelier MA, Reneman L. The age-dependent effects of a single-dose methylphenidate challenge on cerebral perfusion in patients with attention-deficit/hyperactivity disorder. Neuroimage Clin. 2017;13:123–129.
37. Rao H, Wang J, Giannetta J, et al. Altered resting cerebral blood flow in adolescents with in utero cocaine exposure revealed by perfusion functional MRI. Pediatrics. 2007;120:e1245–e1254.
38. Wang J, Licht DJ. Pediatric perfusion MRI with arterial spin labeling. Neuroimaging Clin North America. 2006;16:149–167.
39. Alsop DC, Detre JA, Golay X, et al. Recommended implementation of arterial spin-labeled perfusion MRI for clinical applications: a consensus of the ISMRM perfusion study group and the European consortium for ASL in dementia. Magn Reson Med. 2015;73:102–116.
40. Martin SZ, Madai VI, von Samson-Himmelstjerna FC, et al. 3D GRASE pulsed arterial spin labeling at multiple inflow times in patients with long arterial transit times: comparison with dynamic susceptibility-weighted contrast-enhanced MRI at 3 Tesla. J Cereb Blood Flow Metab. 2015;35:392–401.
41. Vidorreta M, Wang Z, Chang YV, Wolk DA, Fernandez-Seara MA, Detre JA. Whole-brain background-suppressed pCASL MRI with 1D-accelerated 3D RARE Stack-Of-Spirals readout. PLoS One. 2017;12:e0183762.
42. Grade M, Hernandez Tamames JA, Pizzini FB, Achten E, Golay X, Smits M. A neuroradiologist's guide to arterial spin labeling MRI in clinical practice. Neuroradiology. 2015;57:1181–1202.
43. Petersen ET, Zimine I, Ho YC, Golay X. Non-invasive measurement of perfusion: a critical review of arterial spin labelling techniques. Br J Radiol. 2006;79:688–701.
44. Yun TJ, Sohn CH, Yoo RE, et al. Transit time corrected arterial spin labeling technique aids to overcome delayed transit time effect. Neuroradiology. 2018;60:255–265.
45. Qin Q, Huang AJ, Hua J, Desmond JE, Stevens RD, van Zijl PC. Three-dimensional whole-brain perfusion quantification using pseudo-continuous arterial spin labeling MRI at multiple post-labeling delays: accounting for both arterial transit time and impulse response function. NMR Biomed. 2014;27:116–128.
46. Wolf ME, Layer V, Gregori J, et al. Assessment of perfusion deficits in ischemic stroke using 3D-GRASE arterial spin labeling magnetic resonance imaging with multiple inflow times. J Neuroimaging. 2014;24:453–459.
47. Boland M, Stirnberg R, Pracht ED, et al. Accelerated 3D-GRASE imaging improves quantitative multiple post labeling delay arterial spin labeling. Magn Reson Med. 2018;80:2475–2484.
48. Dai W, Robson PM, Shankaranarayanan A, Alsop DC. Reduced resolution transit delay prescan for quantitative continuous arterial spin labeling perfusion imaging. Magn Reson Med. 2012;67:1252–1265.
49. Federau C, Christensen S, Zun Z, et al. Cerebral blood flow, transit time, and apparent diffusion coefficient in moyamoya disease before and after acetazolamide. Neuroradiology. 2017;59:5–12.
50. Wang R, Yu S, Alger JR, et al. Multi-delay arterial spin labeling perfusion MRI in moyamoya disease–comparison with CT perfusion imaging. Eur Radiol. 2014;24:1135–1144.
51. Wang DJ, Alger JR, Qiao JX, et al. Multi-delay multi-parametric arterial spin-labeled perfusion MRI in acute ischemic stroke - Comparison with dynamic susceptibility contrast enhanced perfusion imaging. Neuroimage Clin. 2013;3:1–7.
52. Lou X, Yu S, Scalzo F, et al. Multi-delay ASL can identify leptomeningeal collateral perfusion in endovascular therapy of ischemic stroke. Oncotarget. 2017;8:2437–2443.
53. Chen G, Lei D, Ren J, et al. Patterns of postictal cerebral perfusion in idiopathic generalized epilepsy: a multi-delay multi-parametric arterial spin labelling perfusion MRI study. Sci Rep. 2016;6:28867.
54. Hu HH, Rusin JA, Peng R, et al. Multi-phase 3D arterial spin labeling brain MRI in assessing cerebral blood perfusion and arterial transit times in children at 3T. Clin Imaging. 2019;53:210–220.
55. Mithal LB, Patel PS, Mithal D, Palac HL, Rozenfeld MN. Use of gadolinium-based magnetic resonance imaging contrast agents and awareness of brain gadolinium deposition among pediatric providers in North America. Pediatr Radiol. 2017;47:657–664.
56. Soares BP, Lequin MH, Huisman T. Safety of contrast material use in children. Magn Reson Imaging Clin N Am. 2017;25:779–785.
57. Brucher N, Vial J, Baunin C, et al. Non-contrast-enhanced MR angiography using time-spin labelling inversion pulse technique for detecting crossing renal vessels in children with symptomatic ureteropelvic junction obstruction: comparison with surgical findings. Eur Radiol. 2016;26:2697–2704.
58. Zhou Z, Han F, Yu S, et al. Accelerated noncontrast-enhanced 4-dimensional intracranial MR angiography using golden-angle stack-of-stars trajectory and compressed sensing with magnitude subtraction. Magn Reson Med. 2018;79:867–878.
59. Hu HH, Pokorney AL, Stefani N, Chia JM, Miller JH. Non-gadolinium dynamic angiography of the neurovasculature using arterial spin labeling MRI: preliminary experience in children. MAGMA. 2017;30:107–112.
60. Nakamura M, Yoneyama M, Tabuchi T, et al. Vessel-selective, non-contrast enhanced, time-resolved MR angiography with vessel-selective arterial spin labeling technique (CINEMA-SELECT) in intracranial arteries. Radiol Phys Technol. 2013;6:327–334.
61. Togao O, Hiwatashi A, Obara M, et al. 4D ASL-based MR angiography for visualization of distal arteries and leptomeningeal collateral vessels in moyamoya disease: a comparison of techniques. Eur Radiol. 2018;28:4871–4881.
62. Thawait SK, Chaudhry V, Thawait GK, et al. High-resolution MR neurography of diffuse peripheral nerve lesions. AJNR Am J Neuroradiol. 2011;32:1365–1372.
63. Upadhyaya V, Upadhyaya DN, Mishra B. MR neurography in traumatic, non-obstetric paediatric brachial plexopathy. Eur Radiol. 2018;28:2417–2424.
64. Chhabra A, Belzberg AJ, Rosson GD, et al. Impact of high resolution 3 tesla MR neurography (MRN) on diagnostic thinking and therapeutic patient management. Eur Radiol. 2016;26:1235–1244.
65. Cortes C, Ramos Y, Restrepo R, Restrepo JA, Grossman JA, Lee EY. Practical magnetic resonance imaging evaluation of peripheral nerves in children: magnetic resonance neurography. Radiol Clin North Am. 2013;51:673–688.
66. Merlini L, Vargas MI, Anooshiravani M, Viallon M, Fluss J, Hanquinet S. Look for the nerves! MR neurography adds essential diagnostic value to routine MRI in pediatric practice: a pictorial overview. J Neuroradiol. 2011;38:141–147.
67. Andreisek G, Crook DW, Burg D, Marincek B, Weishaupt D. Peripheral neuropathies of the median, radial, and ulnar nerves: MR imaging features. Radiographics. 2006;26:1267–1287.
68. Bendszus M, Koltzenburg M, Wessig C, Solymosi L. Sequential MR imaging of denervated muscle: experimental study. AJNR Am J Neuroradiol. 2002;23:1427–1431.
69. Bendszus M, Wessig C, Reiners K, Bartsch AJ, Solymosi L, Koltzenberg M. MR imaging in the differential diagnosis of neurogenic foot drop. AJNR Am J Neuroradiol. 2003;24:1283–1289.
70. Chhabra A, Williams EH, Wang KC, Dellon AL, Carrino JA. MR neurography of neuromas related to nerve injury and entrapment with surgical correlation. AJNR Am J Neuroradiol. 2010;31:1363–1368.
71. Filler AG, Kliot M, Howe FA, et al. Application of magnetic resonance neurography in the evaluation of patients with peripheral nerve pathology. J Neurosurg. 1996;85:299–309.
72. Filler AG, Haynes J, Jordan SE, et al. Sciatica of nondisc origin and piriformis syndrome: diagnosis by magnetic resonance neurography and interventional magnetic resonance imaging with outcome study of resulting treatment. J Neurosurg Spine. 2005;2:99–115.
73. Andreisek G, Burg D, Studer A, Weishaupt D. Upper extremity peripheral neuropathies: role and impact of MR imaging on patient management. Eur Radiol. 2008;18:1953–1961.
74. Fisher S, Wadhwa V, Manthuruthil C, Cheng J, Chhabra A. Clinical impact of magnetic resonance neurography in patients with brachial plexus neuropathies. Br J Radiol. 2016;89:20160503.
75. Howe FA, Filler AG, Bell BA, Griffiths JR. Magnetic resonance neurography. Magn Reson Med. 1992;28:328–338.
76. Chhabra A, Lee PP, Bizzell C, Soldatos T. 3 Tesla MR neurography–technique, interpretation, and pitfalls. Skeletal Radiol. 2011;40:1249–1260.
77. Karampinos DC, Melkus G, Shepherd TM, et al. Diffusion tensor imaging and T2 relaxometry of bilateral lumbar nerve roots: feasibility of in-plane imaging. NMR Biomed. 2013;26:630–637.
78. Simon NG, Lagopoulos J, Gallagher T, Kliot M, Kiernan MC. Peripheral nerve diffusion tensor imaging is reliable and reproducible. J Magn Reson Imaging. 2016;43:962–969.
79. van der Jagt PK, Dik P, Froeling M, et al. Architectural configuration and microstructural properties of the sacral plexus: a diffusion tensor MRI and fiber tractography study. Neuroimage. 2012;62:1792–1799.
80. Kakuda T, Fukuda H, Tanitame K, et al. Diffusion tensor imaging of peripheral nerve in patients with chronic inflammatory demyelinating polyradiculoneuropathy: a feasibility study. Neuroradiology. 2011;53:955–960.
81. Mathys C, Aissa J, Meyer Zu Horste G, et al. Peripheral neuropathy: assessment of proximal nerve integrity by diffusion tensor imaging. Muscle Nerve. 2013;48:889–896.
82. Kasper JM, Wadhwa V, Scott KM, Rozen S, Xi Y, Chhabra A. SHINKEI–a novel 3D isotropic MR neurography technique: technical advantages over 3DIRTSE-based imaging. Eur Radiol. 2015;25:1672–1677.
83. Yoneyama M, Takahara T, Kwee TC, Nakamura M, Tabuchi T. Rapid high resolution MR neurography with a diffusion-weighted pre-pulse. Magn Reson Med Sci. 2013;12:111–119.

84. Wang X, Harrison C, Mariappan YK, et al. MR neurography of brachial plexus at 3.0 t with robust fat and blood suppression. Radiology. 2017;283:538–546.
85. Li K, Dortch RD, Welch EB, et al. Multi-parametric MRI characterization of healthy human thigh muscles at 3.0 T - relaxation, magnetization transfer, fat/water, and diffusion tensor imaging. NMR Biomed. 2014;27:1070–1084.
86. Cervantes B, Kirschke JS, Klupp E, et al. Orthogonally combined motion- and diffusion-sensitized driven equilibrium (OC-MDSDE) preparation for vessel signal suppression in 3D turbo spin echo imaging of peripheral nerves in the extremities. Magn Reson Med. 2018;79:407–415.
87. Chhabra A, Soldatos T, Subhawong TK, et al. The application of three-dimensional diffusion-weighted PSIF technique in peripheral nerve imaging of the distal extremities. J Magn Reson Imaging. 2011;34:962–967.
88. Madhuranthakam AJ, Lenkinski RE. Technical advancements in MR neurography. Semin Musculoskelet Radiol. 2015;19:86–93.
89. Busse RF. Flow Sensitivity of CPMG Sequences with Variable Flip Refocusing and Implications for CSF Signal Uniformity in 3D-FSE Imaging. Seattle, Washington, USA. In: Proceedings of the 14th Annual Meeting of ISMRM. 2006:2430.
90. Cervantes B, Hu HH, Pokorney A, et al. CSF-Free Imaging of the Lumbar Plexus using Sub-Millimeter Resolutions with 3D TSE. Singapore, Singapore. In: Proceedings of the 24th Annual Meeting of ISMRM. 2016:2250.
91. Hajnal JV, Bryant DJ, Kasuboski L, et al. Use of fluid attenuated inversion recovery (FLAIR) pulse sequences in MRI of the brain. J Comput Assist Tomogr. 1992;16:841–844.
92. Cervantes B, Bauer JS, Zibold F, et al. Imaging of the lumbar plexus: Optimized refocusing flip angle train design for 3D TSE. J Magn Reson Imaging. 2016;43:789–799.
93. Wu B, Warnock G, Zaiss M, et al. An overview of CEST MRI for non-MR physicists. EJNMMI Phys. 2016;3:19.
94. Xu J, Zaiss M, Zu Z, et al. On the origins of chemical exchange saturation transfer (CEST) contrast in tumors at 9.4 T. NMR Biomed. 2014;27:406–416.
95. Zhou J, Lal B, Wilson DA, Laterra J, van Zijl PC. Amide proton transfer (APT) contrast for imaging of brain tumors. Magn Reson Med. 2003;50:1120–1126.
96. Zhao X, Wen Z, Zhang G, et al. Three-dimensional turbo-spin-echo amide proton transfer MR imaging at 3-Tesla and its application to high-grade human brain tumors. Mol Imaging Biol. 2013;15:114–122.
97. Holmes HE, Colgan N, Ismail O, et al. Imaging the accumulation and suppression of tau pathology using multiparametric MRI. Neurobiol Aging. 2016;39:184–194.
98. Kim M, Kim HS. Emerging techniques in brain tumor imaging: What radiologists need to know. Korean J Radiol. 2016;17:598–619.
99. Togao O, Kessinger CW, Huang G, et al. Characterization of lung cancer by amide proton transfer (APT) imaging: an in-vivo study in an orthotopic mouse model. PLoS One. 2013;8:e77019.
100. Bai Y, Lin Y, Zhang W, et al. Noninvasive amide proton transfer magnetic resonance imaging in evaluating the grading and cellularity of gliomas. Oncotarget. 2017;8:5834–5842.
101. Togao O, Yoshiura T, Keupp J, et al. Amide proton transfer imaging of adult diffuse gliomas: correlation with histopathological grades. Neuro Oncol. 2014;16:441–448.
102. Togao O, Hiwatashi A, Yamashita K, et al. Grading diffuse gliomas without intense contrast enhancement by amide proton transfer MR imaging: comparisons with diffusion- and perfusion-weighted imaging. Eur Radiol. 2017;27:578–588.
103. Park JE, Lee JY, Kim HS, et al. Amide proton transfer imaging seems to provide higher diagnostic performance in post-treatment high-grade gliomas than methionine positron emission tomography. Eur Radiol. 2018;28:3285–3295.
104. Yu H, Lou H, Zou T, et al. Applying protein-based amide proton transfer MR imaging to distinguish solitary brain metastases from glioblastoma. Eur Radiol. 2017;27:4516–4524.
105. Togao O, Hiwatashi A, Keupp J, et al. Scan-rescan reproducibility of parallel transmission based amide proton transfer imaging of brain tumors. J Magn Reson Imaging. 2015;42:1346–1353.
106. Ma X, Bai Y, Lin Y, et al. Amide proton transfer magnetic resonance imaging in detecting intracranial hemorrhage at different stages: a comparative study with susceptibility weighted imaging. Sci Rep. 2017;7:45696.
107. Jeong HK, Han K, Zhou J, et al. Characterizing amide proton transfer imaging in haemorrhage brain lesions using 3T MRI. Eur Radiol. 2017;27:1577–1584.
108. Joo B, Han K, Choi YS, et al. Amide proton transfer imaging for differentiation of benign and atypical meningiomas. Eur Radiol. 2018;28:331–339.
109. Zhou J, van Zijl PC. Defining an acidosis-based ischemic penumbra from pH-weighted MRI. Transl Stroke Res. 2011;3:76–83.
110. Sun PZ, Zhou J, Sun W, Huang J, van Zijl PC. Detection of the ischemic penumbra using pH-weighted MRI. J Cereb Blood Flow Metab. 2007;27:1129–1136.
111. Wu Y, Zhou IY, Lu D, et al. pH-sensitive amide proton transfer effect dominates the magnetization transfer asymmetry contrast during acute ischemia-quantification of multipool contribution to in vivo CEST MRI. Magn Reson Med. 2018;79:1602–1608.
112. Tietze A, Blicher J, Mikkelsen IK, et al. Assessment of ischemic penumbra in patients with hyperacute stroke using amide proton transfer (APT) chemical exchange saturation transfer (CEST) MRI. NMR Biomed. 2014;27:163–174.
113. Zheng Y, Wang X, Zhao X. Magnetization transfer and amide proton transfer MRI of neonatal brain development. Biomed Res Int. 2016;2016:3052723.
114. Zhang H, Kang H, Zhao X, et al. Amide proton transfer (APT) MR imaging and magnetization transfer (MT) MR imaging of pediatric brain development. Eur Radiol. 2016;26:3368–3376.
115. Tang XZH, Zhao X, Zhou J, Peng Y. Assessment of brain development in children with developmental delay using amide proton transfer weighted (APTw) MRI. Proc Int Soc Magn Reson Med. 2016;24:3698.
116. Wang R, Li SY, Chen M, et al. Amide proton transfer magnetic resonance imaging of Alzheimer's disease at 3.0 Tesla: a preliminary study. Chin Med J (Engl). 2015;128:615–619.
117. McDonald CM, Henricson EK, Abresch RT, et al. The 6-minute walk test and other endpoints in Duchenne muscular dystrophy: longitudinal natural history observations over 48 weeks from a multicenter study. Muscle Nerve. 2013;48:343–356.
118. Tuffery-Giraud S, Saquet C, Chambert S, et al. The role of muscle biopsy in analysis of the dystrophin gene in Duchenne muscular dystrophy: experience of a national referral centre. Neuromuscul Disord. 2004;14:650–658.
119. Kinali M, Arechavala-Gomeza V, Cirak S, et al. Muscle histology vs MRI in Duchenne muscular dystrophy. Neurology. 2011;76:346–353.
120. Willis TA, Hollingsworth KG, Coombs A, et al. Quantitative muscle MRI as an assessment tool for monitoring disease progression in LGMD2I: a multicentre longitudinal study. PLoS One. 2013;8:e70993.
121. Simon NG, Noto YI, Zaidman CM. Skeletal muscle imaging in neuromuscular disease. J Clin Neurosci. 2016;33:1–10.
122. Mul K, Vincenten SCC, Voermans NC, et al. Adding quantitative muscle MRI to the FSHD clinical trial toolbox. Neurology. 2017;89:2057–2065.
123. Fatehi F, Salort-Campana E, Le Troter A, Bendahan D, Attarian S. Muscle MRI of facioscapulohumeral dystrophy (FSHD): A growing demand and a promising approach. Rev Neurol (Paris). 2016;172:566–571.
124. Tasca G, Monforte M, Ottaviani P, et al. Magnetic resonance imaging in a large cohort of facioscapulohumeral muscular dystrophy patients: Pattern refinement and implications for clinical trials. Ann Neurol. 2016;79:854–864.
125. Gerevini S, Scarlato M, Maggi L, et al. Muscle MRI findings in facioscapulohumeral muscular dystrophy. Eur Radiol. 2016;26:693–705.
126. Li W, Zheng Y, Zhang W, Wang Z, Xiao J, Yuan Y. Progression and variation of fatty infiltration of the thigh muscles in Duchenne muscular dystrophy, a muscle magnetic resonance imaging study. Neuromuscul Disord. 2015;25:375–380.
127. Finanger EL, Russman B, Forbes SC, Rooney WD, Walter GA, Vandenborne K. Use of skeletal muscle MRI in diagnosis and monitoring disease progression in Duchenne muscular dystrophy. Phys Med Rehabil Clin N Am. 2012;23:1–10, ix.
128. Hollingsworth KG, de Sousa PL, Straub V, Carlier PG. Towards harmonization of protocols for MRI outcome measures in skeletal muscle studies: consensus recommendations from two TREAT-NMD NMR workshops, 2 May 2010, Stockholm, Sweden, 1-2 October 2009, Paris, France. Neuromuscul Disord. 2012;22 Suppl 2:S54–S67.
129. Mercuri E, Pichiecchio A, Allsop J, Messina S, Pane M, Muntoni F. Muscle MRI in inherited neuromuscular disorders: past, present, and future. J Magn Reson Imaging. 2007;25:433–440.
130. Morrow JM, Matthews E, Raja Rayan DL, et al. Muscle MRI reveals distinct abnormalities in genetically proven non-dystrophic myotonias. Neuromuscul Disord. 2013;23:637–646.
131. Marty B, Coppa B, Carlier PG. Monitoring skeletal muscle chronic fatty degenerations with fast T1-mapping. Eur Radiol. 2018;28:4662–4668.
132. Marty B, Baudin PY, Reyngoudt H, et al. Simultaneous muscle water T2 and fat fraction mapping using transverse relaxometry with stimulated echo compensation. NMR Biomed. 2016;29:431–443.
133. Carlier PG, Marty B, Scheidegger O, et al. Skeletal muscle quantitative nuclear magnetic resonance imaging and spectroscopy as an outcome measure for clinical trials. J Neuromuscul Dis. 2016;3:1–28.
134. Damon BM, Li K, Dortch RD, et al. Quantitative magnetic resonance imaging of skeletal muscle disease. J Vis Exp. 2016;118.
135. Forbes SC, Willcocks RJ, Rooney WD, Walter GA, Vandenborne K. MRI quantifies neuromuscular disease progression. Lancet Neurol. 2016;15:26–28.
136. Morrow JM, Sinclair CD, Fischmann A, et al. MRI biomarker assessment of neuromuscular disease progression: a prospective observational cohort study. Lancet Neurol. 2016;15:65–77.
137. Johnston JH, Kim HK, Merrow AC, et al. Quantitative skeletal muscle MRI: Part 1, derived T2 fat map in differentiation between boys with Duchenne muscular dystrophy and healthy boys. AJR Am J Roentgenol. 2015;205:W207–W215.
138. Kim HK, Serai S, Lindquist D, et al. Quantitative skeletal muscle MRI: Part 2, MR spectroscopy and T2 relaxation time mapping-comparison between boys with Duchenne muscular dystrophy and healthy boys. AJR Am J Roentgenol. 2015;205:W216–W223.
139. Karampinos DC, Ruschke S, Dieckmeyer M, et al. Quantitative MRI and spectroscopy of bone marrow. J Magn Reson Imaging. 2018;47:332–353.
140. Battaglia M, Rimondi E, Monti C, et al. Validity of T2 mapping in characterization of the regeneration tissue by bone marrow derived cell transplantation in osteochondral lesions of the ankle. Eur J Radiol. 2011;80:e132–e139.
141. Cordes C, Baum T, Dieckmeyer M, et al. MR-based assessment of bone marrow fat in osteoporosis, diabetes, and obesity. Front Endocrinol (Lausanne). 2016;7:74.

142. Kim PK, Hong YJ, Im DJ, et al. Myocardial T1 and T2 mapping: Techniques and clinical applications. Korean J Radiol. 2017;18:113–131.
143. Kellman P, Hernando D, Arai AE. Myocardial fat imaging. Curr Cardiovasc Imaging Rep. 2010;3:83–91.
144. Tang A, Tan J, Sun M, et al. Nonalcoholic fatty liver disease: MR imaging of liver proton density fat fraction to assess hepatic steatosis. Radiology. 2013;267:422–431.
145. Reeder SB, Cruite I, Hamilton G, Sirlin CB. Quantitative assessment of liver fat with magnetic resonance imaging and spectroscopy. J Magn Reson Imaging. 2011;34(4). spcone.
146. Yokoo T, Serai SD, Pirasteh A, et al. Linearity, bias, and precision of hepatic proton density fat fraction measurements by using MR imaging: a meta-analysis. Radiology. 2018;286:486–498.
147. Hu HH, Kan HE. Quantitative proton MR techniques for measuring fat. NMR Biomed. 2013;26:1609–1629.
148. Reeder SB, Cruite I, Hamilton G, Sirlin CB. Quantitative assessment of liver fat with magnetic resonance imaging and spectroscopy. J Magn Reson Imaging. 2011;34:729–749.
149. Burakiewicz J, Sinclair CDJ, Fischer D, Walter GA, Kan HE, Hollingsworth KG. Quantifying fat replacement of muscle by quantitative MRI in muscular dystrophy. J Neurol. 2017;264:2053–2067.
150. Ponrartana S, Ramos-Platt L, Wren TA, et al. Effectiveness of diffusion tensor imaging in assessing disease severity in Duchenne muscular dystrophy: preliminary study. Pediatr Radiol. 2015;45:582–589.
151. Horvath JJ, Austin SL, Case LE, et al. Correlation between quantitative whole-body muscle magnetic resonance imaging and clinical muscle weakness in Pompe disease. Muscle Nerve. 2015;51:722–730.
152. Janssen BH, Voet NB, Nabuurs CI, et al. Distinct disease phases in muscles of facioscapulohumeral dystrophy patients identified by MR detected fat infiltration. PLoS One. 2014;9:e85416.
153. Mankodi A, Azzabou N, Bulea T, et al. Skeletal muscle water T2 as a biomarker of disease status and exercise effects in patients with Duchenne muscular dystrophy. Neuromuscul Disord. 2017;27:705–714.
154. Wokke BH, Van Den Bergen JC, Hooijmans MT, Verschuuren JJ, Niks EH, Kan HE. T2 relaxation times are increased in Skeletal muscle of DMD but not BMD patients. Muscle Nerve. 2016;53:38–43.
155. Kan HE, Scheenen TW, Wohlgemuth M, et al. Quantitative MR imaging of individual muscle involvement in facioscapulohumeral muscular dystrophy. Neuromuscul Disord. 2009;19:357–362.
156. Tawara N, Nitta O, Kuruma H, Niitsu M, Itoh A. T2 mapping of muscle activity using ultrafast imaging. Magn Reson Med Sci. 2011;10:85–91.
157. Patten C, Meyer RA, Fleckenstein JL. T2 mapping of muscle. Semin Musculoskelet Radiol. 2003;7:297–305.
158. Carlier PG, Azzabou N, de Sousa PL, et al. Skeletal muscle quantitative nuclear magnetic resonance imaging follow-up of adult Pompe patients. J Inherit Metab Dis. 2015;38:565–572.
159. Ruschke S, Kienberger H, Baum T, et al. Diffusion-weighted stimulated echo acquisition mode (DW-STEAM) MR spectroscopy to measure fat unsaturation in regions with low proton-density fat fraction. Magn Reson Med. 2016;75:32–41.
160. Janiczek RL, Gambarota G, Sinclair CD, et al. Simultaneous T(2) and lipid quantitation using IDEAL-CPMG. Magn Reson Med. 2011;66:1293–1302.
161. CAA E, Azzabou N, Vignaud A, Guillot G, Carlier PG. Quantitative ultrashort TE imaging of the short-T2 components in skeletal muscle using an extended echo-subtraction method. Magn Reson Med. 2017;78:997–1008.
162. Loughran T, Higgins DM, McCallum M, Coombs A, Straub V, Hollingsworth KG. Improving highly accelerated fat fraction measurements for clinical trials in muscular dystrophy: origin and quantitative effect of R2* changes. Radiology. 2015;275:570–578.
163. Hollingsworth KG, Higgins DM, McCallum M, Ward L, Coombs A, Straub V. Investigating the quantitative fidelity of prospectively undersampled chemical shift imaging in muscular dystrophy with compressed sensing and parallel imaging reconstruction. Magn Reson Med. 2014;72:1610–1619.
164. Bitar R, Leung G, Perng R, et al. MR pulse sequences: what every radiologist wants to know but is afraid to ask. Radiographics. 2006;26:513–537.
165. Moratal D, Valles-Luch A, Marti-Bonmati L, Brummer M. k-Space tutorial: an MRI educational tool for a better understanding of k-space. Biomed Imaging Interv J. 2008;4:e15.
166. Paschal CB, Morris HD. K-space in the clinic. J Magn Reson Imaging. 2004;19:145–159.
167. Deshmane A, Gulani V, Griswold MA, Seiberlich N. Parallel MR imaging. J Magn Reson Imaging. 2012;36:55–72.
168. Hamilton J, Franson D, Seiberlich N. Recent advances in parallel imaging for MRI. Prog Nucl Magn Reson Spectrosc. 2017;101:71–95.
169. Jaspan ON, Fleysher R, Lipton ML. Compressed sensing MRI: a review of the clinical literature. Br J Radiol. 2015;88:20150487.
170. European Society of Radiology (ESR). Magnetic Resonance Fingerprinting - a promising new approach to obtain standardized imaging biomarkers from MRI. Insights Imaging. 2015;6:163–165.
171. Otazo R, Kim D, Axel L, Sodickson DK. Combination of compressed sensing and parallel imaging for highly accelerated first-pass cardiac perfusion MRI. Magn Reson Med. 2010;64:767–776.
172. Fritz J, Fritz B, Zhang J, et al. Simultaneous multislice accelerated turbo spin echo magnetic resonance imaging: comparison and combination with in-plane parallel imaging acceleration for high-resolution magnetic resonance imaging of the knee. Invest Radiol. 2017;52:529–537.
173. Bo Z, Bilgic B, Adalsteinsson E, Griswold MA, Wald LL, Setsompop K. Simultaneous multislice magnetic resonance fingerprinting with low-rank and subspace modeling. Conf Proc IEEE Eng Med Biol Soc. 2017;2017:3264–3268.
174. Moeller S, Yacoub E, Olman CA, et al. Multiband multislice GE-EPI at 7 tesla, with 16-fold acceleration using partial parallel imaging with application to high spatial and temporal whole-brain fMRI. Magn Reson Med. 2010;63:1144–1153.
175. Cohen AD, Nencka AS, Wang Y. Multiband multi-echo simultaneous ASL/BOLD for task-induced functional MRI. PLoS One. 2018;13:e0190427.
176. Schulz J, P Marques J, Ter Telgte A, et al. Clinical application of half fourier acquisition single shot turbo spin echo (HASTE) imaging accelerated by simultaneous multi-slice acquisition. Eur J Radiol. 2018;98:200–206.
177. Feinberg DA, Setsompop K. Ultra-fast MRI of the human brain with simultaneous multi-slice imaging. J Magn Reson. 2013;229:90–100.
178. Marami B, Scherrer B, Afacan O, Warfield SK, Gholipour A. Motion-robust reconstruction based on simultaneous multi-slice registration for diffusion-weighted MRI of moving subjects. Med Image Comput Comput Assist Interv. 2016;9902:544–552.
179. Ye H, Cauley SF, Gagoski B, et al. Simultaneous multislice magnetic resonance fingerprinting (SMS-MRF) with direct-spiral slice-GRAPPA (ds-SG) reconstruction. Magn Reson Med. 2017;77:1966–1974.
180. Feinberg DA, Beckett A, Chen L. Arterial spin labeling with simultaneous multi-slice echo planar imaging. Magn Reson Med. 2013;70:1500–1506.
181. Chen L, TV A, Xu J, et al. Evaluation of highly accelerated simultaneous multi-slice EPI for fMRI. Neuroimage. 2015;104:452–459.
182. Todd N, Moeller S, Auerbach EJ, Yacoub E, Flandin G, Weiskopf N. Evaluation of 2D multiband EPI imaging for high-resolution, whole-brain, task-based fMRI studies at 3T: sensitivity and slice leakage artifacts. Neuroimage. 2016;124(Pt A):32–42.
183. Barth M, Breuer F, Koopmans PJ, Norris DG, Poser BA. Simultaneous multislice (SMS) imaging techniques. Magn Reson Med. 2016;75:63–81.
184. Feinberg DA, Yacoub E. The rapid development of high speed, resolution and precision in fMRI. Neuroimage. 2012;62:720–725.
185. Poser BA, Setsompop K. Pulse sequences and parallel imaging for high spatiotemporal resolution MRI at ultra-high field. Neuroimage. 2018;168:101–118.
186. Glasser MF, Smith SM, Marcus DS, et al. The Human Connectome Project's neuroimaging approach. Nat Neurosci. 2016;19:1175–1187.
187. Geethanath S, Reddy R, Konar AS, et al. Compressed sensing MRI: a review. Crit Rev Biomed Eng. 2013;41:183–204.
188. Smith DS, Li X, Abramson RG, Quarles CC, Yankeelov TE, Welch EB. Potential of compressed sensing in quantitative MR imaging of cancer. Cancer Imaging. 2013;13:633–644.
189. Roy CW, Seed M, Kingdom JC, Macgowan CK. Motion compensated cine CMR of the fetal heart using radial undersampling and compressed sensing. J Cardiovasc Magn Reson. 2017;19:29.
190. Zhou Z, Han F, Rapacchi S, et al. Accelerated ferumoxytol-enhanced 4D multiphase, steady-state imaging with contrast enhancement (MUSIC) cardiovascular MRI: validation in pediatric congenital heart disease. NMR Biomed. 2017;30(1).
191. Bao S, Tamir JI, Young JL, et al. Fast comprehensive single-sequence four-dimensional pediatric knee MRI with T2 shuffling. J Magn Reson Imaging. 2017;45:1700–1711.
192. Zhang T, Chowdhury S, Lustig M, et al. Clinical performance of contrast enhanced abdominal pediatric MRI with fast combined parallel imaging compressed sensing reconstruction. J Magn Reson Imaging. 2014;40:13–25.
193. Zhang T, Yousaf U, Hsiao A, et al. Clinical performance of a free-breathing spatiotemporally accelerated 3-D time-resolved contrast-enhanced pediatric abdominal MR angiography. Pediatr Radiol. 2015;45:1635–1643.
194. Blystad I, Warntjes JB, Smedby O, Landtblom AM, Lundberg P, Larsson EM. Synthetic MRI of the brain in a clinical setting. Acta Radiol. 2012;53:1158–1163.
195. McAllister A, Leach J, West H, Jones B, Zhang B, Serai S. Quantitative synthetic MRI in children: normative intracranial tissue segmentation values during development. AJNR Am J Neuroradiol. 2017;38:2364–2372.
196. Park S, Kwack KS, Lee YJ, Gho SM, Lee HY. Initial experience with synthetic MRI of the knee at 3T: comparison with conventional T1 weighted imaging and T2 mapping. Br J Radiol. 2017;90:20170350.
197. Tanenbaum LN, Tsiouris AJ, Johnson AN, et al. Synthetic MRI for clinical neuroimaging: results of the magnetic resonance image compilation (MAGiC) prospective, multicenter, multireader trial. AJNR Am J Neuroradiol. 2017;38:1103–1110.
198. Lee SM, Choi YH, Cheon JE, et al. Image quality at synthetic brain magnetic resonance imaging in children. Pediatr Radiol. 2017;47:1638–1647.
199. West H, Leach JL, Jones BV, et al. Clinical validation of synthetic brain MRI in children: initial experience. Neuroradiology. 2017;59:43–50.
200. Betts AM, Leach JL, Jones BV, Zhang B, Serai S. Brain imaging with synthetic MR in children: clinical quality assessment. Neuroradiology. 2016;58:1017–1026.
201. Ma D, Gulani V, Seiberlich N, et al. Magnetic resonance fingerprinting. Nature. 2013;495:187–192.

202. Pouliot P, Gagnon L, Lam T, et al. Magnetic resonance fingerprinting based on realistic vasculature in mice. Neuroimage. 2017;149:436–445.
203. Christen T, Pannetier NA, Ni WW, et al. MR vascular fingerprinting: A new approach to compute cerebral blood volume, mean vessel radius, and oxygenation maps in the human brain. Neuroimage. 2014;89: 262–270.
204. Wright KL, Jiang Y, Ma D, et al. Estimation of perfusion properties with MR fingerprinting arterial spin labeling. Magn Reson Imaging. 2018;50: 68–77.
205. Badve C, Yu A, Dastmalchian S, et al. MR fingerprinting of adult brain tumors: Initial experience. AJNR Am J Neuroradiol. 2017;38:492–499.
206. Su P, Mao D, Liu P, et al. Multiparametric estimation of brain hemodynamics with MR fingerprinting ASL. Magn Reson Med. 2017;78:1812–1823.
207. Warntjes JB, Leinhard OD, West J, Lundberg P. Rapid magnetic resonance quantification on the brain: optimization for clinical usage. Magn Reson Med. 2008;60:320–329.
208. West J, Warntjes JB, Lundberg P. Novel whole brain segmentation and volume estimation using quantitative MRI. Eur Radiol. 2012;22:998–1007.
209. Warntjes M, Engstrom M, Tisell A, Lundberg P. Modeling the presence of myelin and edema in the brain based on multi-parametric quantitative MRI. Front Neurol. 2016;7:16.
210. Olchowy C, Cebulski K, Lasecki M, et al. The presence of the gadolinium-based contrast agent depositions in the brain and symptoms of gadolinium neurotoxicity - A systematic review. PLoS One. 2017;12:e0171704.
211. Smith AB, Gupta N, Strober J, Chin C. Magnetic resonance neurography in children with birth-related brachial plexus injury. Pediatr Radiol. 2008;38: 159–163.
212. Jaimes C, Kirsch JE, Gee MS. Fast, free-breathing and motion-minimized techniques for pediatric body magnetic resonance imaging. Pediatr Radiol. 2018;48:1197–1208.
213. Parad RB. Non-sedation of the neonate for radiologic procedures. Pediatr Radiol. 2018;48:524–530.
214. Barkovich MJ, Xu D, Desikan RS, Williams C, Barkovich AJ. Pediatric neuro MRI: tricks to minimize sedation. Pediatr Radiol. 2018;48:50–55.
215. Arlachov Y, Ganatra RH. Sedation/anaesthesia in paediatric radiology. Br J Radiol. 2012;85:e1018–e1031.